



**HAL**  
open science

## **A Deep Alteration and Oxidation Profile in a Shallow Clay Aquitard: Example of the Tégulines Clay, East Paris Basin, France**

Catherine Lerouge, Jean-Charles Robinet, Mathieu Debure, Christophe Tournassat, Alain Bouchet, Ana Fernandez, Christine Fléhoc, Catherine Guerrot, Myriam Kars, France Lagroix, et al.

► **To cite this version:**

Catherine Lerouge, Jean-Charles Robinet, Mathieu Debure, Christophe Tournassat, Alain Bouchet, et al.. A Deep Alteration and Oxidation Profile in a Shallow Clay Aquitard: Example of the Tégulines Clay, East Paris Basin, France. *Geofluids*, 2018, 2018, pp.1 - 20. 10.1155/2018/1606753 . insu-01719398

**HAL Id: insu-01719398**

**<https://insu.hal.science/insu-01719398>**






Submitted on 28 Feb 2018

**HAL** is a multi-disciplinary open access archive for the deposit and dissemination of scientific research documents, whether they are published or not. The documents may come from teaching and research institutions in France or abroad, or from public or private research centers.

L'archive ouverte pluridisciplinaire **HAL**, est destinée au dépôt et à la diffusion de documents scientifiques de niveau recherche, publiés ou non, émanant des établissements d'enseignement et de recherche français ou étrangers, des laboratoires publics ou privés.

## Research Article

# A Deep Alteration and Oxidation Profile in a Shallow Clay Aquitard: Example of the Tégulines Clay, East Paris Basin, France

Catherine Lerouge <sup>1</sup>, Jean-Charles Robinet,<sup>2</sup> Mathieu Debure <sup>1</sup>,  
Christophe Tournassat,<sup>1,3,4</sup> Alain Bouchet,<sup>5</sup> Ana María Fernández,<sup>6</sup> Christine Flehoc,<sup>1</sup>  
Catherine Guerrot,<sup>1</sup> Myriam Kars,<sup>7</sup> France Lagroix,<sup>8</sup> Philippe Landrein <sup>2</sup>,  
Benoit Madé,<sup>2</sup> Philippe Negrel,<sup>1</sup> Guillaume Wille <sup>1</sup> and Francis Claret <sup>1</sup>

<sup>1</sup>BRGM, BP36009, 45060 Orléans Cedex 2, France

<sup>2</sup>ANDRA, 1-7 rue Jean-Monnet, 92298 Châtenay-Malabry Cedex, France

<sup>3</sup>UMR 7327 Institut des Sciences de la Terre d'Orléans (ISTO), Université d'Orléans-CNRS/INSU-BRGM, Orléans, France

<sup>4</sup>Energy Geoscience Division, Lawrence Berkeley National Laboratory, 1 Cyclotron Rd., Berkeley, CA 94720, USA

<sup>5</sup>ERM, Bâtiment B8, 7 rue Albert Turpain, 86000 Poitiers, France

<sup>6</sup>CIEMAT, Departamento de Medio Ambiente, 28040 Madrid, Spain

<sup>7</sup>Center for Advanced Marine Core Research, Kochi University, B200 Monobe, Nankoku 783-8502, Japan

<sup>8</sup>Institut de Physique du Globe de Paris (IPGP), Paris, France

Correspondence should be addressed to Catherine Lerouge; [c.lerouge@brgm.fr](mailto:c.lerouge@brgm.fr)

Received 12 June 2017; Revised 23 September 2017; Accepted 11 December 2017; Published 23 January 2018

Academic Editor: Douglas K. Solomon

Copyright © 2018 Catherine Lerouge et al. This is an open access article distributed under the Creative Commons Attribution License, which permits unrestricted use, distribution, and reproduction in any medium, provided the original work is properly cited.

The oxidation profile of a surficial clay aquitard was studied on a 35-meter borecore from the Albian Tégulines Clay near Brienne-le-Château (Paris Basin, France). Mineralogical, geochemical, and petrophysical data showed evidences of gradual oxidation taking place down to a depth of 20 m. Below 20 m, the clay material was nonplastic and nonfractured, and it inherited reduced redox conditions from bacterial sulfate reduction that occurred after sediment deposition. Above 20 m, the clay material was plastic. Up to a depth of 10–11 m, only rare yellowish aggregates of glauconite attested to limited oxidation, and pore water chemistry was unmodified. The 5–11 m depth interval was characterized by intensive pyrite oxidation, calcite dissolution, and formation of sulfate and iron hydroxide minerals. The upper 2–3 m was ochrous and entirely oxidized. These mineralogical changes were mirrored with pore water chemistry modifications such as an increase of alkalinity and sulfate concentration in the upper part of the profile. The presence of siderite at ~11 m evinced the reactivity of Fe(II) in the structure of clay minerals with dioxygen from meteoric waters that infiltrated into the Tégulines Clay through vertical fractures.

## 1. Introduction

Clay-rich geological formations act as natural low permeability protective barriers preventing contamination of groundwater resources due to extremely long time scales for groundwater flow and solute transport and the capacity of clay minerals to fix cationic contaminants [1–6]. Determining transport mechanisms (advection/diffusion) is first important for evaluating and modelling how contaminants migrate

through a geological formation. One way of characterizing the transport mechanisms is to study the vertical profiles of natural conservative tracers in pore waters, such as oxygen and hydrogen isotopes, and dissolved halogens such as chlorine [4, 5]. When tracer concentrations do not vary vertically, the dominant transport mechanism may be advection [3], whereas curvilinear concentration profiles suggest that diffusion dominates [1–4]. In addition to the relevant transport regime, how speciation occurs during transport

is of utmost importance because it will determine how mobile tracers are. Among parameters that affect speciation, redox potential is a crucial one for predicting the mobility of redox-sensitive chemical elements. Most of the clay-rich geological formations studied in the scope of waste disposal were deposited in marine environments under suboxic to reduced conditions [4, 7, 8]. They are generally sandwiched by limestones and/or sandstones that act as aquifers through which present-day waters (meteoric/ground waters) slowly penetrate. In deep environments, transition zones between reduced clay formations and oxic aquifers do not clearly give evidence of oxidation/reduction reactivity due to water/rock interactions, which means that the propagation of an oxidation front from the aquifer to a deep clay formation may be very limited. In surficial and shallow environments, the proximity of an atmosphere that is an infinite oxygen reservoir and the small distance for meteoric waters to penetrate into the formation induce mineral, chemical, petrophysical, and mechanical changes in clay-rocks. Weathering induces spatially extensive or discontinuous heterogeneities such as fractures [9–11] and uncompacted sand layers [9], or changes to pore water chemistry and alkalinity, pyrite oxidation, and sulfur state change [6], and changes in other redox proxies such as Ce, Mn, and U [12–16]. These can create perturbations in transport flow paths and rates. Lateral advective solute transport is frequently described in near-surface fractured and oxidized zones of aquitards [10, 17]. However, how far the oxidized layers extend vertically remains unclear.

In the context of surface repository for low level nuclear waste, the Lower Cretaceous Gault clay formation is a near-surface aquitard that Andra (the French National Radioactive Waste Management Agency) has begun to investigate in the area of Brienne-le-Château (north-eastern France). They carried out a dedicated investigation of Gault clay through two drilling campaigns in 2013 and 2015 to characterize its chemical, mineral, petrological, and textural properties and its present-day pore water chemistry. Because of the low permeability and diffusivity of the rock, which hinders the propagation of reaction fronts, the weathering and oxidation profiles as well as the presence of sharp redox fronts were expected to be limited. The main objectives of this work were to define the redox profile of the Gault Clay based on a complete mineralogical (distribution of redox-sensitive minerals), geochemical (redox-sensitive elements such as Fe and S), and petrophysical dataset and to identify the major factors controlling the present-day Tégulines pore water chemistry. This is the first attempt to construct a conceptual model for solute transport in the near-surface Gault clay aquitard and to support performance evaluations.

## 2. Geological Setting

The studied area of Brienne-le-Château (Aube department) is located in the eastern part of the Paris Basin. The Gault clay formation in the studied area consists of siliciclastic shales deposited in an open marine environment at the maximum flooding surface [25] from Middle to Upper Albian (Lower Cretaceous) on the Greensands formation [26] (Figure 1). Temperatures of deep marine waters during Albian were

estimated at around 13–18°C [27]. The limit between Greensands and Gault clay is a major truncative unconformity. An important hiatus between the Aptian and the Albian formations exists in the Aube stratotype due to a general low sea level of eustatic origin [28]. The area that we have studied is the most subsident one in the Paris Basin. The stratotype of the Gault clay defined in the Aube department consists of Argiles Tégulines de Courcelles (82 m) (in the following referred to as Tégulines Clay) overlaid by the Marnes de Brienne (43 m).

The Tégulines Clay consists of three successive facies which are from bottom to top: (1) phosphatic nodule beds, (2) silty clays, and (3) clays and limestone beds. The Marnes de Brienne consists of (1) clay marls, (2) gaize, and (3) clay marls. Phosphatic nodule beds [31], hardgrounds, and glauconitic and sandy beds and layers rich in fossils [32] are currently described in the Tégulines Clay [25]. Several phosphatic nodule beds are continuous over more than 130 km, to Aube in the southwest and Perthois in the northeast. They are interpreted as Flooding Surfaces of 3rd-order cycles [25].

Thick successions of chalk deposited over the Gault clay during Cenomanian-Turonian and Campanian-Maastrichtian transgressions of Late Cretaceous times [33]. Then the basin emerged at the Cretaceous-Tertiary limit, allowing the progressive exhumation of the underlying Gault clay sediments. The retreat of the Upper Cretaceous Sea defined the primitive river network to the east of Paris. The rivers developed on the Cretaceous marine regression surface retreating to the north. Therefore, the rivers appeared sooner in the south and later in the north [34]. At –23 Ma (Early Miocene), the Paris Basin was eroded and similar to the present day. Nowadays the Gault clay formation outcrops as an 8–10 km wide and 80-km long band of terranes oriented NE-SW through the Aube department in the eastern part of the Paris Basin (Figure 1(a)). The thickness increases from east to west between 60 and 120 m, indicating that the total thickness of Upper Cretaceous and Tertiary sediments overlying the Gault clay, and a part of the Gault clay itself, was eroded.

The maximum burial in the Paris Basin was reached during the Upper Cretaceous [35], but the total thickness of the sediments that overlaid the Gault clay in the studied area remains approximate (Figure 1(b)). About 700 m of Late Cretaceous chalk and Tertiary sediments were crosscut by drilling at Poigny, southeast of Paris [36], and 700 m is also the thickness evaluated in the Brie Plaine [33] or in Champagne [35], 600 m in the eastern Paris Basin [37], and  $400 \pm 300$  m in south-eastern Paris Basin [38]. Thermal models indicate thickness of 300–350 m of Late Cretaceous chalk near Troyes based on fluid inclusion microthermometry [39] and 400–600 m near Saint Dizier based on organic matter [40]. Assuming a thickness of about 300–600 m of sediments overlying the Gault clay and a surface temperature of  $\sim 23 \pm 2^\circ\text{C}$  [37], the maximum burial temperature did not exceed 30–36°C. During the Late Tertiary and Quaternary most of the continent emerged, and the disappearance of the sea influence induced general climatic cooling. During the Quaternary the glacial and interglacial periods alternated and influenced erosion and weathering processes.

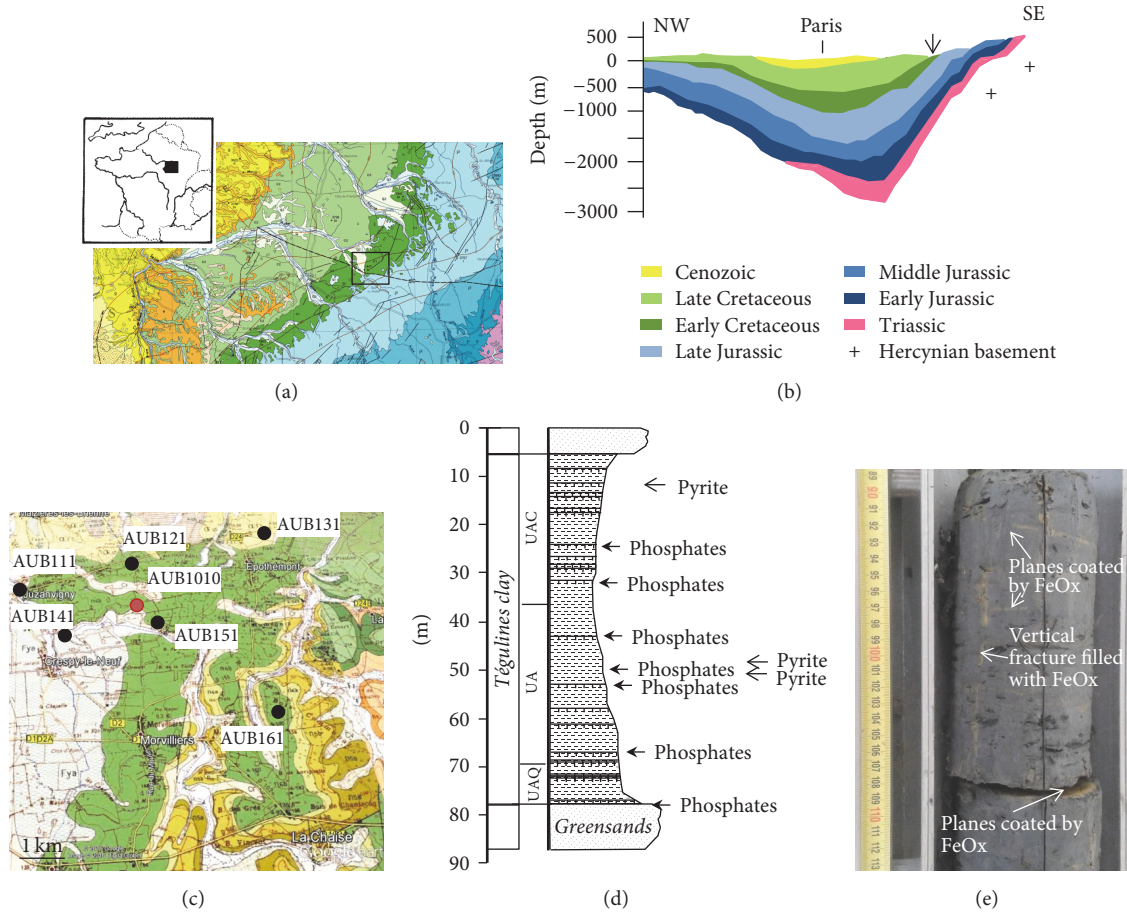


FIGURE 1: (a) Geological map of the eastern part of the Paris Basin showing the study area; (b) NW-SE schematic cross-section of the Paris Basin according to the Gonçalvès et al. hydro-thermo-mechanical model [18]. The Gault clay is a part of the dark green area. (c) Geological map of the area studied and location of the boreholes. (d) Schema of the lithostratigraphic sequence of the Gault clay in the area of Brienne-le-Château based on the boreholes AUB111 and AUB121 for which the thickness of the clay is largest. (e) Vertical fracture filled with Fe hydroxides (FeOx) crosscutting core sample AUB1010-9.25 m.

### 3. Materials and Methods

**3.1. Drilling Campaigns, Lithology of Tégulines Clay, and Sampling.** Albian Gault clay formation in the area east of Brienne-le-Château was studied for its mineralogy, its chemistry, and its petrophysical properties. More than 70 samples were collected from six different boreholes (referenced AUB111, AUB121, AUB131, AUB141, AUB151, and AUB161) from the 2013 drilling campaign and of one borehole (referenced AUB1010) from the 2015 drilling campaign (Figure 1(c)). All boreholes were drilled through surficial formations and the Gault clay down to Greensands. Surficial formations were between 0.7 and 6 m thick and consisted of sands, silty clay, and reworked calcareous materials. The Gault clay was only represented by the Tégulines Clay; the Brienne marls were absent. The thickness of the Tégulines Clay crosscut by the seven boreholes ranged between 0 and 80 m, which was influenced by the low dipping of 1° from southeast to northwest. The thickness was highest in the AUB111 and AUB121 boreholes (65–75 m) located in the northwest of the studied area near Juzanvigny, of ~35–40 m in AUB141 and AUB1010 boreholes, ~25–30 m in AUB131 and AUB151

boreholes, and minimal in the AUB161 borehole (<10 m) in the southeast. Aptian Greensands were uncompacted glauconitic quartz sands; however at their upper levels in contact with Tégulines Clay, 0.35 to 1 meters of sand was consolidated. It had quite even thickness of ~6–10 m in the seven boreholes.

The lithology of the Tégulines Clay was established on the basis of the observations of the AUB111 and AUB121 boreholes for which the formation thickness was the highest (Andra 2015) (Figure 1(d)). The bottom of the clay formation (defined as the UAQ unit) consisted of a 4–5 m thick green silty layer rich in coarse quartz grains and in glauconite at the bottom, followed by 5–7 m of successive small sedimentary cycles of black silty claystones and glauconite-rich silty claystone limited by a bioturbated surface at the top. This was overlain by ~35–40 m thick dark claystones rich in bioturbations (defined as the UA unit) and containing some layers rich in phosphate nodules. The top of the formation (defined as the UAC unit) only present in boreholes AUB111 and AUB121 consisted of a 20–25 m thick dark grey claystone containing decimeter-thick carbonate layers near the transition with the Brienne marls. Numerous mm to cm sized phosphate

TABLE 1: Types of characterization, analytical methods, and conditioning used for each type of characterization.

| Objectives                              | Type of analyses   | Conditioning    |
|---|--|-----------------|
| Bulk rock chemistry                     | Major elements (X-ray fluorescence)  | Liquid nitrogen |
|   | $\text{Fe}^{2+}/\text{Fe}^{3+}$  |                 |
|   | TOC  |                 |
| Petrophysical properties of rock        | Sulfides/sulfates  | Aluminum bag    |
|   | Gravimetric water content  |                 |
|   | Densitometry   |                 |
| Pore water chemistry                    | Mercury intrusion/extrusion tests  | Aluminum bag    |
|   | Major cations, anions on water extracted by squeezing  |                 |
| Pore water chemistry (indirect methods) | $\delta^{18}\text{O}$ , $\delta\text{D}$ on degassed water at 70°C   | Glass container |
|   | Leaching tests with MilliQ water: anion (Cl and sulfate), CEC using cobalt hexammine method: major cations, Sr and $^{87}\text{Sr}/^{86}\text{Sr}$ | Liquid nitrogen |
| Rock mineralogy                         | XRD, SEM, EPMA, IRM  | Liquid nitrogen |
| Isotopic geochemistry                   | (C, O) Stable isotopes on carbonates, $^{87}\text{Sr}/^{86}\text{Sr}$ on carbonates  | Liquid nitrogen |

TOC, total organic carbon; CEC, cation exchange capacity; XRD, X-ray diffraction; SEM, scanning electron microscope; EPMA, electron probe microanalyzer; IRM, isothermal remanent magnetization.

nodules occurred at different levels of the clay formation crosscut in boreholes (Figure 1(d)), which is consistent with literature [31]. Pyrite was not macroscopically identified in the core samples because of its small size, but rare centimeter-thick nodules and bioturbations were observed in borehole AUB111, at depth 22.0 m and in borehole AUB1010 at depths 6.63 m and 8.25 m (Figure 1(d)).

Weathering of the Tégulines Clay was visible macroscopically on the core samples, marked by the presence of iron hydroxides and gypsum, and a yellowish rock color. These changes affected the surficial part of the clay formation at variable depths in boreholes: ~3-4 m for boreholes AUB111, AUB121, AUB131, and AUB141, ~10 m for boreholes AUB151 and AUB1010, and ~22 m for borehole AUB161. In this last borehole, the Tégulines Clay was thin, and the weathering also affected the underlying Greensands. In the AUB1010 borehole at 9.25 m, iron hydroxides were evidenced as filling both a subvertical mm thick fracture perpendicular to the bedding, as well as coating planes in the clay-rock bedding (Figure 1(e)).

**3.2. Sample Conditioning and Analytical Techniques.** The cores were conditioned immediately after being removed from the core sampler to minimize atmospheric contact. The list of analyses and the type of conditioning adapted to the analyses are given in Table 1 and the analytical methods are detailed in Supplementary Appendix 1. Samples conditioned in a Dewar flask containing liquid  $\text{N}_2$  (77 K) on the field were directly lyophilized at laboratory. An intact piece of rock of each sample was embedded in a resin for thin section preparation and the remaining parts were crushed into fine-grained powder ( $<80\ \mu\text{m}$ ) and stored in a glove box under  $\text{N}_2$  atmosphere. Samples conditioned in double-layered heat-sealed plasticized aluminum bags under vacuum. These bags were stored in glove boxes under  $\text{N}_2$  atmosphere in the laboratory facilities until analyses.

## 4. Rock Characterization

All the major mineralogical, chemical, and isotopic data of clay-rocks are given in Supplementary Appendix 2 (xls file).

**4.1. Lithology and Mineralogy.** Main mineralogy based on XRD analysis and bulk major element chemistry was obtained for the 77 Tégulines Clay samples. The clay formation consisted dominantly of clay fraction (35–66 wt.% with a mean value of 51 wt.%) associated with quartz-feldspar silty fraction (18–58 wt.% with a mean value of 36 wt.%) and a calcite-dominant carbonate fraction (0–30 wt.% with a mean value of 9 wt.%). Accessory minerals representing less than 5 wt.% of the rock were dolomite, ankerite, siderite, pyrite, and gypsum. Siderite was only a major mineral in sample AUB1010-11.32 m. Total organic carbon was very low and almost homogeneous ( $0.5 \pm 0.1$  wt.%). Bulk iron content in the Tégulines Clay was homogeneous at the scale of the formation (~5 wt.% equivalent  $\text{Fe}_2\text{O}_3$ ). The  $\text{Fe}^{2+}/(\text{Fe}^{2+} + \text{Fe}^{3+})$  ratios of bulk clay-rocks from the AUB1010 borehole are ~0.8 below 11.32 m and ~0.2 above.

Mineral variability in the Tégulines Clay was mainly vertical without major lateral variations. We compared the overall vertical variability on the basis of the quantified mineralogy of samples from the AUB111 and AUB121 boreholes for which the Tégulines Clay was thickest, and the three main mineral units are represented (Figure 2).

At the bottom of the clay formation, the 9–12 m thick clay-quartz rich unit (UAQ) was characterized by the highest quartz-feldspar silty content (32–62% with a mean value of 46%) and the lowest carbonate content (0–12 wt.% with a mean value of 3.5 wt.%), a value of almost 0 at its bottom. At the top of the clay formation, the 20–25 m thick carbonate-clay-rich unit (UAC) was characterized by the highest carbonate content (9–25 wt.% with a mean value of 17 wt.%) and the lowest quartz-feldspar silty content (21–52 wt.% with a mean value of 30 wt.%). The intermediate 35–40 m thick clay-rich unit (UA unit) was characterized by the highest clay

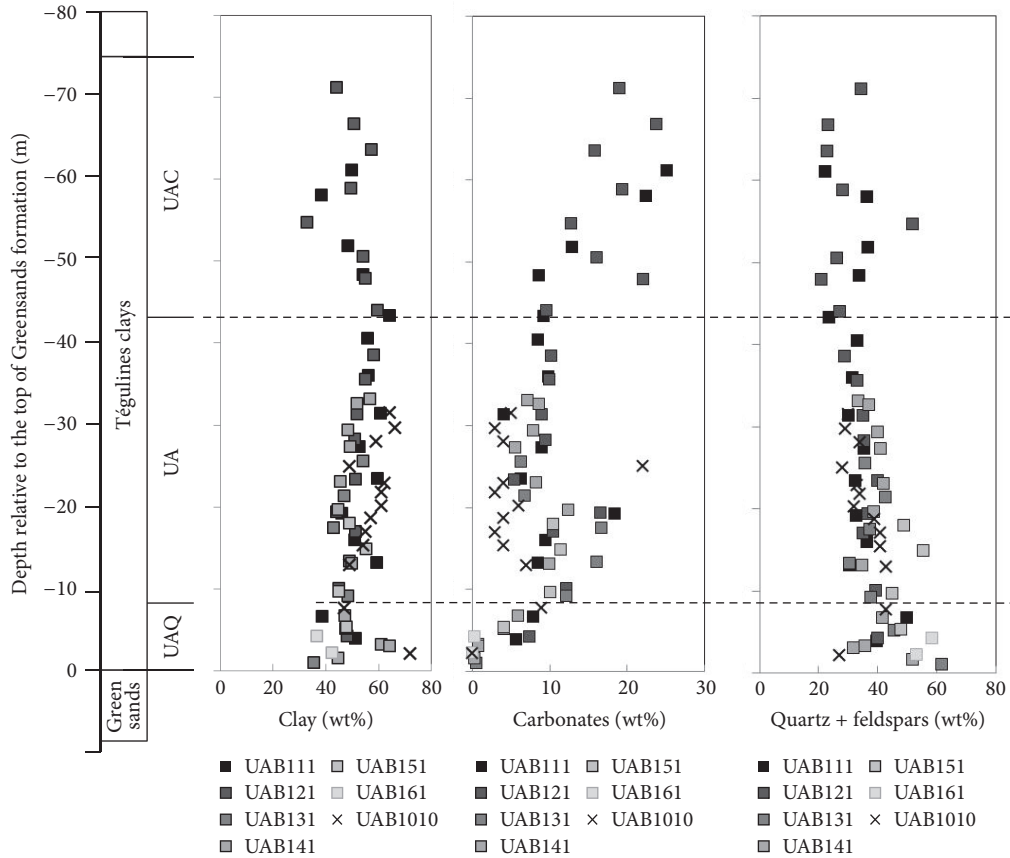


FIGURE 2: Profiles of clay, carbonates, and (quartz + K-feldspar) silty contents as a function of depth relative to the top of Greensands. Dashed lines indicate the limits of the three units defined in the Tégulines Clay.

average content of 51 wt.% and intermediate carbonate and quartz-feldspar silty contents.

**4.1.1. Clay Minerals.** Toward the surface, in the first meters of the Tégulines Clay, the ochre color replaced the greenish color, because of the oxidation of iron in clay minerals. The clay fraction of the Tégulines Clay was composed of a quite homogeneous fine-grained matrix of illite-micas ( $12 \pm 5$  wt.%), glauconite ( $8 \pm 6$  wt.%), illite-smectite mixed layers minerals ( $16 \pm 4$  wt.%), and kaolinite ( $16 \pm 5$  wt.%), with minor chlorite ( $<2$  wt.%) (Figure 3(a)). The few samples poor in kaolinite and one sample poor in illite/micas/glauconite were from the bottom part of the clay formation (UAQ clay-quartz unit). The glauconite content was high and varied a lot at the extremities of the Tégulines Clay (Figure 3(b)). Under the microscope, the clay fraction was composed of dominant  $<2 \mu\text{m}$  clay particles with minor  $50 \mu\text{m}$  sized flakes of white mica, biotite (Figure 3(c)), and chlorite (Figure 3(d)) of detrital origin. Glauconite was diagenetic and occurred as 50 to  $200 \mu\text{m}$  sized greenish to yellowish rounded aggregates (Figure 3(f)).

Chemical compositions of the  $<2 \mu\text{m}$  clay matrix reported in the  $4\text{Si}-\text{M}^+-\text{R}^{2+}$  diagram modified from Meunier and Velde [19] corresponded dominantly to the field of illite and illite-smectite mixed layers; some others were aligned between the montmorillonite endmember and the

chlorite endmember suggesting smectite-chlorite mixing (Figure 3(e)). Some chemical compositions of the  $<2 \mu\text{m}$  clay matrix in the AUB131-5 m sample near the surface evolve to the beidellite endmember [19]. This chemical evolution corresponds to a depletion of divalent cations in the clays, probably due to the iron oxidation. Flakes of white mica were on the line between muscovite and phengite. Chlorite flakes generally contained traces of titanium and potassium, strongly suggesting that chlorite derived from biotite alteration. Chemical compositions of glauconite through the Tégulines Clay from the AUB1010 borehole were reported in the  $\text{M}^+ \cdot (\text{Si}/4)^{-1}$  versus  ${}^{\text{VI}}\text{Fe}(\text{II} + \text{III})/\Sigma^{\text{VI}}$  cations diagram (Figure 3(g)). Rounded aggregates of well-preserved green glauconite had homogeneous compositions belonging to the field of highly evolved Fe-poor glauconite according to [4, 20, 21]. Rounded aggregates of glauconite with yellowish changing color had more heterogeneous chemical compositions giving evidence of a loss of iron and potassium and of an increasing smectite component.

**4.1.2. The Quartz-Feldspar Silty Fraction.** This fraction consisted of dominant quartz ( $34 \pm 9$  wt.%) with minor K-feldspar ( $3 \pm 0.6$  wt.%) generally disseminated in the clay matrix; plagioclase was absent. Quartz was essentially present as detrital angular  $<100 \mu\text{m}$  sized grains. Dissolution features affecting

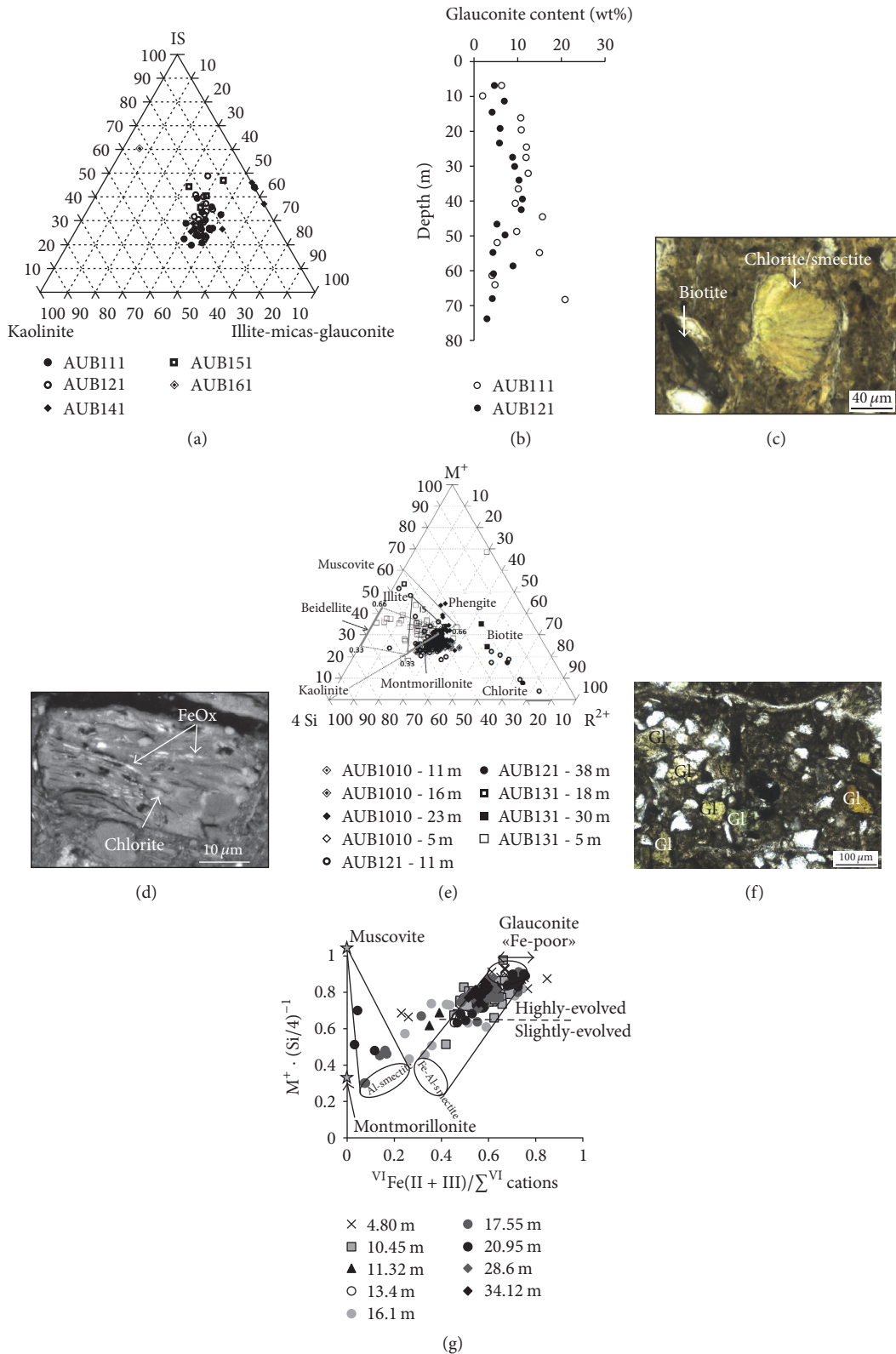


FIGURE 3: (a) Proportions of the major clay minerals reported in a triangular kaolinite (illite-smectite) mixed layers (noted IS) illite/micas/glaucanite. (b) Glauconite content estimated as a function of depth. (c) Chlorite-smectite and biotite flakes (AUB1010-6.63 m) (transmitted light). (d) Chlorite flake with numerous iron hydroxides between the sheets (AUB1010-4.80 m) (BSE image). (e) Electron microprobe analyses of clay minerals of the <2  $\mu\text{m}$  fraction that are reported in a 4Si-M<sup>+</sup>-R<sup>2+</sup> diagram modified from Meunier and Velde [19]. Gray lines indicate the fields of compositions of chlorite, low- (0.33) to high-charge (0.66) beidellites, and of low- (0.33) to high-charge (0.66) montmorillonites. (f) Well-preserved green and brownish oxidized rounded aggregates of glauconite (noted Gl) in sample AUB1010-16.1 m (transmitted light). (g) Electron microprobe analyses of glauconite at different depths of the AUB1010 borehole reported in the M<sup>+</sup> · (Si/4)<sup>-1</sup> versus <sup>VI</sup>Fe(II + III)/ $\Sigma$ <sup>VI</sup> cations diagram indicating compositional domains of glauconite-smectite and illite-smectite according to [20, 21].

detrital grains of K-feldspar were observed in samples toward the surface.

**4.1.3. Carbonates.** The carbonate fraction consisted of bioclasts and of diagenetic carbonates, represented by major calcite with minor dolomite and siderite. Calcitic bioclasts were locally abundant. They were foraminifer tests of few microns and clasts of shells and tests of variable sizes ranging from few microns to centimeters (Figure 4(a)). The largest carbonate shells observed by SEM had almost preserved structures. Diagenetic calcite occurred as micrite disseminated in the clay matrix, often associated with pyrite, and as microsparite that filled residual porosity in bioclasts (Figure 4(b)) and septarian veining in phosphate nodules. Rare dolomite occurred as euhedral grains sometimes surrounded by ankerite corona (Figure 4(c)). In samples near the surface, calcite bioclasts and dolomite showed dissolution features and ankerite was replaced by iron hydroxides (Figure 4(d)). Siderite occurred isolated or as clusters of euhedral transparent grains disseminated in the clay matrix in a few samples (Figure 4(e)) and as a diffuse network of siderite mass impregnating the claystone of the AUB1010-11.32 m sample. Some rare euhedral isolated crystals of siderite were enclosed in diagenetic phosphate nodules (Figure 4(f)). The AUB1010-11.32 m sample corresponded to the change of bulk  $\text{Fe}^{2+}/(\text{Fe}^{2+} + \text{Fe}^{3+})$  ratio in the AUB1010 borehole.

**4.1.4. Phosphate Minerals.** Phosphates occurred as nodules, replacement of bioclasts such as ammonite, or clusters of micron-sized grains of diagenetic phosphate enclosing residual bioclasts, detrital minerals, and other minor diagenetic minerals such as calcite, siderite, pyrite, and glauconite (Figure 4(f)). Some nodules contained pyrite- or calcite-infilled septarian veining very similar to previous observations [31]. From XRD of a phosphate nodule we identified dominant fluorapatite with minor quartz, pyrite, an amorphous phase, and traces of kaolinite and muscovite (Supplementary Appendix 3). The diffractogram was slightly different from those of the fluorapatite reference. The lattice parameters  $a = b$  were estimated at 9.326 Å (instead of 9.3684 Å) and  $c$  at 6.898 Å (instead of 6.881 Å). These variations were consistent with the partial substitution of the  $(\text{PO}_4)^{3-}$  groups by  $(\text{CO}_3)^{2-}$  groups involving the reduction of the tetrahedral coordination in the  $a$ - $b$  plane and low variation along the  $c$  axis. According to [41], the phosphate is so-called francolite and the  $(\text{CO}_3)^{2-}$  content was estimated at 9.2 wt.%.

**4.1.5. Sulfides and Sulfates.** Pyrite was homogeneously present through the Tégulines Clay, except in samples from near the surface. Its content was estimated to 0.8–1.1 wt.% in the different boreholes, with an average value of  $0.9 \pm 0.3$  wt.%. It occurred as isolated framboids, as elongated clusters of framboids disseminated in the clay matrix (Figure 4(e)), as replacement/infillings of bioclasts (Figure 4(b)), and as rare pyrite nodules. Celestite in association with pyrite was identified by SEM in only few samples (Figure 5(h)). Pyrite associated with micrite and dolomite is common early diagenetic mineral formed in the bacterial sulfate reduction (BSR) zones of marine clay formations that evolved in

reducing conditions [7, 8]. Rare celestite associated with framboidal pyrite was probably formed from residual sulfates at the end of the bacterial activity.

Toward the surface, in the first meters of the Tégulines Clay, pyrite was partially to entirely destabilized and replaced by iron hydroxides and gypsum (Figures 5(a), 5(b), 5(d), and 5(e)). The depth limit of visible pyrite oxidation in the AUB1010 borehole corresponded to the change of bulk  $\text{Fe}^{2+}/(\text{Fe}^{2+} + \text{Fe}^{3+})$  ratio, which was  $\sim 0.8$  at 11.32 m and deeper, and decreased down to 0.2 when shallower. Gypsum occurred as coronas surrounding pyrite (AUB1010-8.25 m; Figure 5(h)) and euhedral grains with sizes ranging from 500  $\mu\text{m}$  to 1 mm (Figure 5(g)). A second generation of celestite was observed as filling secondary porosity due to pyrite dissolution (Figure 5(f)). The presence of iron sulfates (probable rhomboclase) was suspected in a cm thick oxidized pyrite analyzed by EDS in SEM and Raman spectrometry. Further investigations are needed to confirm it.

**4.1.6. Iron Hydroxides.** Iron hydroxides were only observed under the microscope in oxidized samples near surface characterized by a low bulk  $\text{Fe}^{2+}/(\text{Fe}^{2+} + \text{Fe}^{3+})$  ratio ( $\sim 0.2$ ). To identify and quantify iron hydroxides formed by weathering, we further investigated seven samples from three boreholes and at different depths (AUB121: 7.9 and 38.4 m, AUB131: 5.5 and 21.8 m, and AUB1010: 6.4, 21.1, and 30.9 m) using magnetic measurements (Supplementary Appendix 4). Low-temperature warming curves of ZFC and FC remanence provided evidence of the presence of magnetite and siderite in samples AUB131-21.75 m, AUB1010-21.10 m, and AUB1010-30.90 m and of increasing goethite content toward the surface. RT-SIRM cycles including a thermal demagnetization stage according to [42] allowed us to determine goethite content in the samples and confirmed the goethite content increase between  $\sim 0.8$  and 2 wt.% (Table 2).

**4.2. Stable Isotopes of Diagenetic Minerals.** We analyzed carbon, oxygen, and strontium isotopes of diagenetic minerals including carbonates and phosphates to determine the origin of the diagenetic fluids from which they precipitated.

The  $^{87}\text{Sr}/^{86}\text{Sr}$  ratio of a calcite bivalve (0.70736) used to characterize pristine marine fluids is consistent with Cretaceous seawater [43]. The  $^{87}\text{Sr}/^{86}\text{Sr}$  ratio of a phosphate nodule (0.70737) is very similar to the signature of initial Albian seawater, indicating the early deposition of phosphates from Albian seawater, in agreement with previous work [31, 44].

Carbon and oxygen isotopic analyses of carbonates were carried out on bulk rock due to the impossibility of separating minerals in clay-rock and consequently represented mixing between different generations of diagenetic carbonates.

The calcite  $\delta^{13}\text{C}$  ranged between 0.4 and 2.9‰<sub>PDB</sub> consistent with the field of marine sedimentary carbonates. The  $\delta^{13}\text{C}$  of all the dolomites (−3.5 to 0.6‰<sub>PDB</sub>) confirmed a marine origin, except the dolomite in sample AUB1010-11.32 m which had a lower  $\delta^{13}\text{C}$  of −5.6‰<sub>PDB</sub>. The siderite  $\delta^{13}\text{C}$  ranged between −11.3 and −7.6‰<sub>PDB</sub> so it was systematically lower than marine values. The  $\delta^{13}\text{C}$  lower than marine



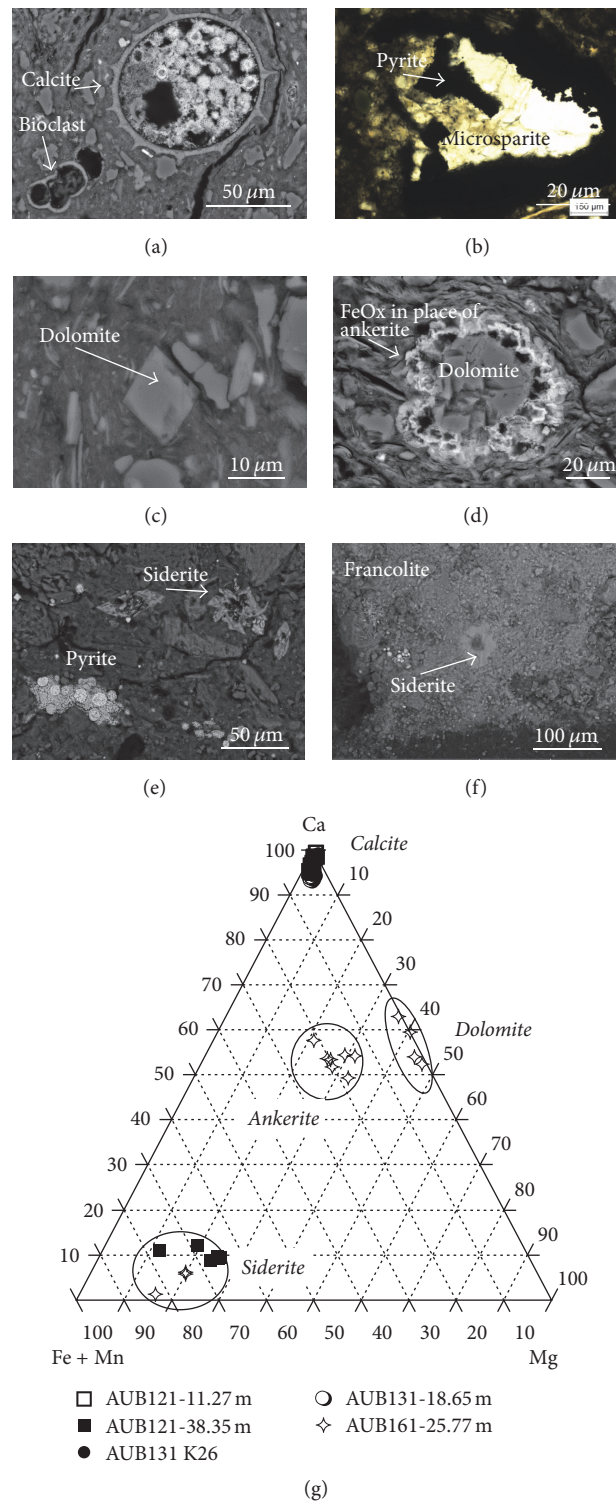


FIGURE 4: (a) Calcite bioclast filled by framboidal pyrite which is partially oxidized (AUB1010-6.63 m) (BSE image); (b) residual porosity in bioclast filled by microsparite (AUB1010-11.32 m) (transmitted light); (c) euhedral grain of dolomite (BSE image) (AUB1010-6.63 m); (d) grain of Fe-bearing dolomite partially dissolved and surrounded by iron hydroxides (BSE image) (AUB1010-4.80 m); (e) cluster of siderite grains (AUB1010-16.1 m); (f) isolated siderite grain enclosed in diagenetic phosphate nodule (AUB131-38 m); (g) electron microprobe analyses of carbonates in thin sections of rock.

TABLE 2: Main results of magnetic remanence measurements: major magnetic Fe-bearing minerals, values of magnetic remanence measured at 300 K during the three successive cycles, loss of remanence between cycles 2 and 3, and estimation of goethite in samples.

|   | AUB131-5.41 m         | AUB131-21.75 m        | AUB1010-6.42 m        | AUB1010-20.1 m                 | AUB1010-30.9 m                  |
|---|-----------------------|-----------------------|-----------------------|--------------------------------|---------------------------------|
| Magnetic minerals                             | Goethite              | Goethite              | Goethite, hematite    | Goethite, magnetite, siderite? | Goethite, magnetite?, siderite? |
| M1 cycle 1 (300 K) Am <sup>2</sup> /kg        | $7.19 \times 10^{-4}$ | $7.34 \times 10^{-4}$ | n.d.                  | $4.25 \times 10^{-3}$          | $6.89 \times 10^{-4}$           |
| M2 cycle 2 (300 K) Am <sup>2</sup> /kg        | $9.16 \times 10^{-4}$ | $1.04 \times 10^{-3}$ | $1.41 \times 10^{-3}$ | $4.44 \times 10^{-3}$          | $9.02 \times 10^{-4}$           |
| M3 cycle 3 (300 K) Am <sup>2</sup> /kg        | $4.24 \times 10^{-4}$ | $4.25 \times 10^{-4}$ | $4.12 \times 10^{-4}$ | $3.82 \times 10^{-3}$          | $4.7 \times 10^{-4}$            |
| Remanence lost between cycles 2 and 3 (300 K) | 46%                   | 52%                   | 29%                   | 14%                            | 52%                             |
| Goethite concentration                        | ~1.95%                | ~1.8%                 | ~2%                   | ~1.24%                         | ~0.8%                           |

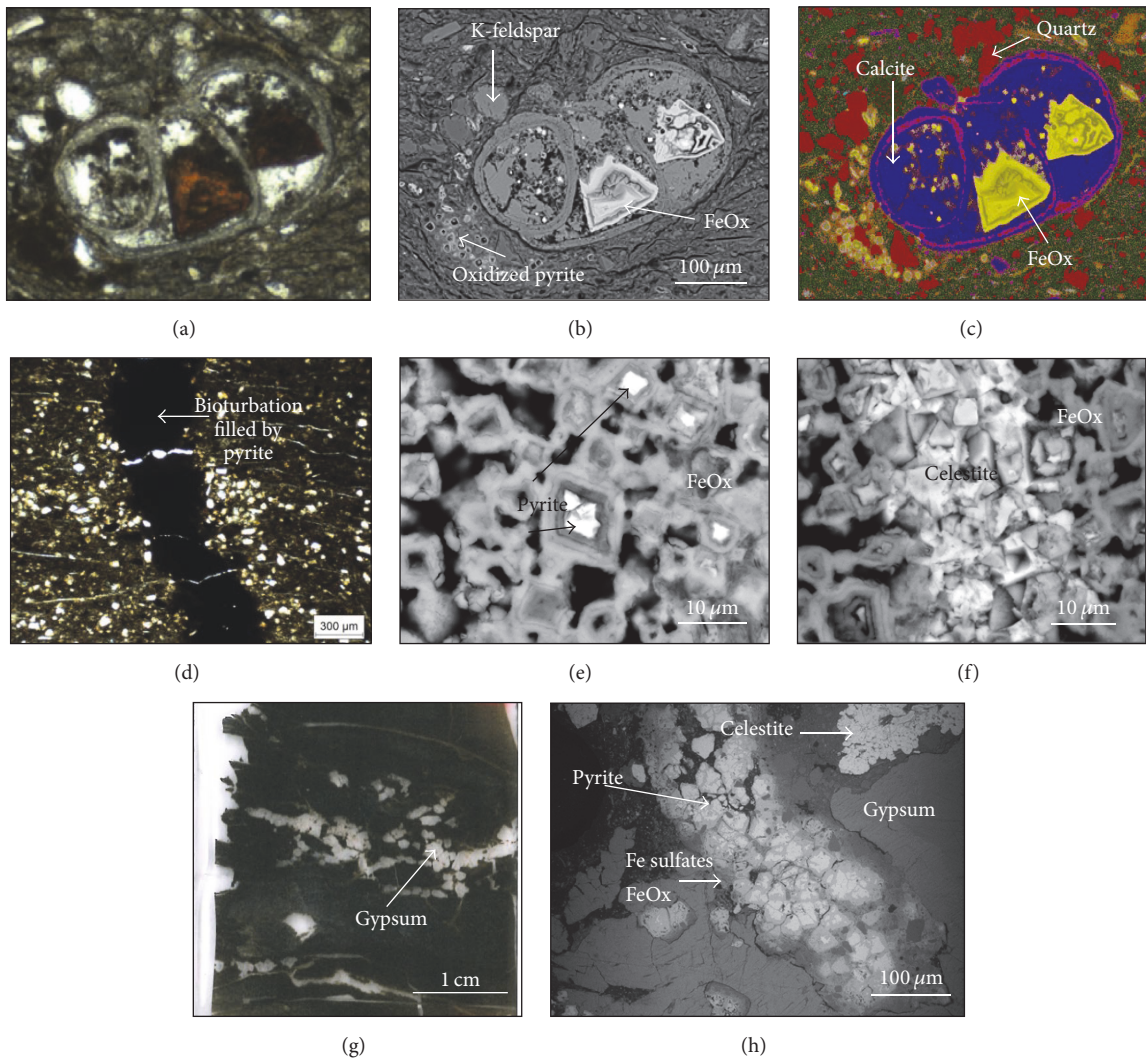


FIGURE 5: Calcite bioclast filled by diagenetic calcite and iron hydroxide (FeOx) replacing pyrite (AUB1010-4.80 m) (a) in transmitted light; (b) in BSE and (c) in chemical composite image (blue: Ca-rich, yellow: Fe rich; red: Si-rich); (d) bioturbation filled by pyrite (AUB1010-6.63 m) (transmitted light); (e) detail of pyrite partially replaced by iron hydroxides (BSE); (f) celestite partially filling zone of pyrite oxidation (BSE); (g) distribution of millimetric gypsum grains replacing pyrite layer in AUB1010-8.25 m (photo of the glass slide); (h) residual diagenetic pyrite and celestite surrounded by secondary iron sulfates, iron hydroxides, and gypsum.

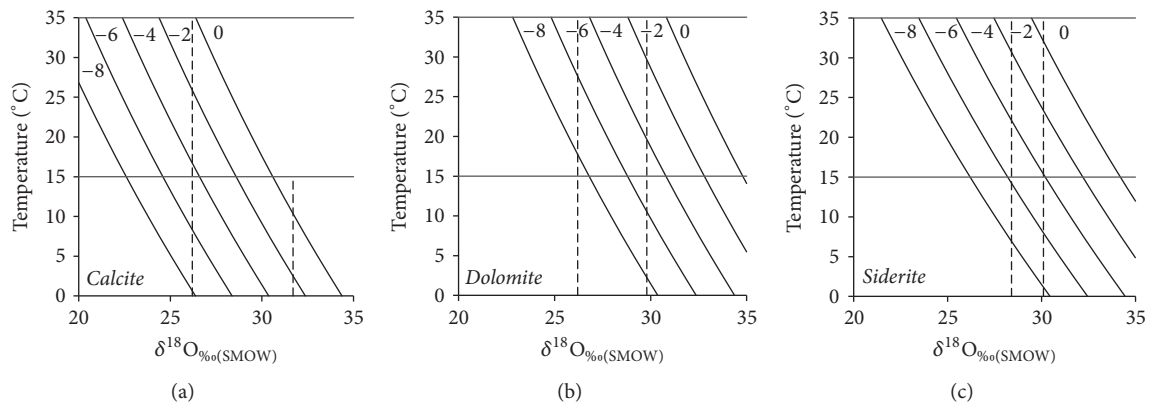


FIGURE 6: Temperature -  $\delta^{18}\text{O}$  diagram in which theoretical curves are reported representing  $\delta^{18}\text{O}$  of calcite (a), dolomite (b), and siderite (c) at equilibrium with a fluid as a function of temperature. Each curve corresponds to a fixed  $\delta^{18}\text{O}_{\text{fluid}}$ .  $\delta^{18}\text{O}_{\text{fluid}}$  of 0‰ SMOW corresponds to seawater,  $\delta^{18}\text{O}_{\text{fluid}}$  ranging from -2 to -8 corresponds to the introduction of meteoric waters in the system. The dotted lines in each diagram indicate the range of the  $\delta^{18}\text{O}$  of analyzed carbonates. The oxygen isotopic fractionations used for the calculations are calcite-water [22], dolomite-water [23], and siderite-water [24].

values measured in the dolomite in sample AUB1010-11.32 m and in all the siderite could be rather due to contribution of an organic component.

The  $\delta^{18}\text{O}$  of calcite (26.2 to 31.7‰<sub>SMOW</sub>), dolomite (26.2 to 29.8‰<sub>SMOW</sub>), and siderite (28.4 to 30.1‰<sub>SMOW</sub>) was close to the marine sedimentary carbonates; however some  $\delta^{18}\text{O}$  variations could be due to weathering. Concerning calcite, the  $\delta^{18}\text{O}$  value of +31.7‰<sub>SMOW</sub> measured in samples from the lower Tégulines Clay was consistent with calcite precipitated from a parent fluid with a  $\delta^{18}\text{O}$  near -1/0‰ (seawater) at ~15°C; however lower values could be also interpreted as resulting of mixing between marine-derived calcite and late calcite precipitated from marine-meteoric mixed waters between 15 and 35°C (Figure 6(a)). Dolomite occurred as early diagenetic mineral present as small amounts and had almost homogeneous  $\delta^{18}\text{O}$  and  $\delta^{13}\text{C}$  through the clay formation, although dolomite/ankerite exhibited dissolution/oxidation in the first ten meters near surface. In unweathered Tégulines Clay, dolomite  $\delta^{18}\text{O}$  of +29/+30‰<sub>SMOW</sub> indicated precipitation from marine-derived waters at maximum burial of 35°C (Figure 6(b)). Siderite occurred as flattened crystals disseminated in unweathered samples of the AUB1010 borehole at 13 and 16 m and had  $\delta^{18}\text{O}$  of +29/ + 30‰<sub>SMOW</sub>. This  $\delta^{18}\text{O}$  range was consistent with a precipitation from marine-derived waters at maximum burial of 35°C (Figure 6(c)). The sample AUB1010-11.32 m was peculiar because it contained a network of massive euhedral siderite (16 wt%) and because calcite, dolomite, and siderite exhibited the lowest  $\delta^{18}\text{O}$  values (Supplementary Appendix 2). The  $^{87}\text{Sr}/^{86}\text{Sr}$  ratio measured in siderite was abnormally high (0.70893) and in the same range as  $^{87}\text{Sr}/^{86}\text{Sr}$  ratio of Tégulines Clay pore waters near surface. The lowest  $\delta^{18}\text{O}$  values of calcite, dolomite, and siderite and the high  $^{87}\text{Sr}/^{86}\text{Sr}$  ratio of siderite probably constituted the record of the infiltration of fluids from surface down to 9 m through fractures. The timing of this event remains unknown.

**4.3. Physical Properties.** Porosity values deduced from the gravimetric water content (porosity 1) and from density measurements (porosity 2) are consistent at the scale of the studied area. They mainly ranged between 25 and 40% with a trend increasing toward the surface (Figure 7). No correlation was evidenced between mineralogy and porosity. In boreholes AUB111 and AUB121 crosscutting the highest thickness of Tégulines Clay, the clay-rock porosity was quite homogenous below 35–40 m, with values of ~25–30%. Above 35–40 m and in all other boreholes for which the thickness of Gault clay was lower than 35–40 m, the clay-rock porosity regularly increased from ~25% up to 35% at 20 m and up to 40% near surface.

The pore size distribution based on mercury intrusion (results not shown) was characterized by dominant pore diameters between 30 and 80 nm in agreement with the clay-rich nature of the samples. The highest values of dominant pore sizes were identified in the samples located near the surface (<20 m) and corresponded also to the highest total porosity. Mercury intrusion porosity was about 20% lower than the density and water content based porosity values. This discrepancy could be explained by the presence of pores inaccessible to mercury (e.g., pores with diameter below 3 nm), mainly interlayer pores related to smectite clay phases [45].

## 5. Pore Water Chemistry

**5.1. Squeezing.** Pore waters were analyzed in seven samples from three boreholes and at different depths: AUB121: 38.05 m (first drilling campaign), AUB131: 21.35 m (first drilling campaign), and AUB1010: 4.8, 10.45, 14.17, 20.95, and 23.39 m (second drilling campaign) (Supplementary Appendix 3). The pH values measured on extracted pore water ranged from 7.6 to 8.2. Alkalinity ranged from 1.2 to 8.2 meq/L. The ionic strength (noted I) was low and varied between 19 and 175 mmol/L. Pore waters in reduced samples from the lower part of the clay formation were characterized by the lowest

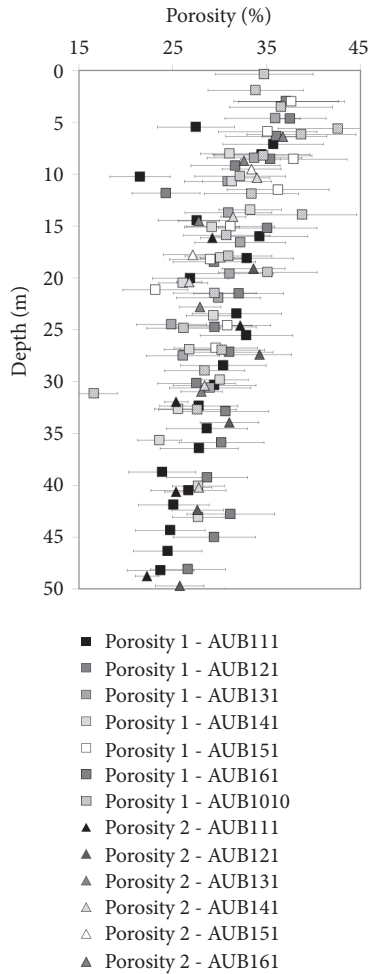


FIGURE 7: Porosities of the core clay samples from the seven boreholes repositioned on a vertical profile as a function of depth.

alkalinity values and the lowest ionic strengths and may be classified as Ca-Mg-sulfate-Cl type waters. Pore waters in weathered samples of the upper part of the clay formation were characterized by increased alkalinity, increased ionic strength values, and evolved to Ca-Mg-sulfate type waters toward the surface.  $S_2O_3^{2-}$  species was only measured in pore waters in samples deeper than 20 m, attesting of reduced conditions. Iron and Al were systematically below the detection limit (0.01 mmol/L).

**5.2. Leaching.** The  $C_{leached,Cl}$  and  $C_{leached,SO_4}$  were measured in leaching of sixteen samples with MilliQ water at three solid/water ratios (10, 20, and 50 g/L). Among them, five samples from the first drilling campaign and eleven samples from the AUB1010 borehole were preserved in liquid nitrogen on the field.  $C_{leached,Cl}$  and  $C_{leached,SO_4}$  were correlated with solid/liquid ratios, suggesting they were not controlled by mineral dissolution/precipitation and adsorption mechanisms.

The  $C_{poro,Cl}$  and  $C_{poro,SO_4}$  deduced from leaching data from the samples from the AUB1010 borehole and the  $C_{bulk,Cl}$  and  $C_{bulk,SO_4}$  obtained by squeezing on few samples

were in the same range of values, showing that the anion accessible porosity was almost similar to the total porosity (Figure 8). Assuming  $C_{poro,i}$  deduced from leaching data as representative of the pore water chemistry ( $C_{bulk,i}$ ), we carried out additional leaching with solid/liquid ratio of 100 g/L on more than thirty samples preserved in aluminum bags under vacuum to complete the anion profiles as a function of depth (Figure 8).

In the lower part of the Tégulines Clay, the  $C_{poro,Cl}$  deduced from the leaching data from all the samples were low (<10 mmol/L PW) and almost consistent, whereas in the upper part of the formation toward the surface, they were more heterogeneous and higher (up to 15 mmol/L PW).

The  $C_{poro,SO_4}$  systematically increased toward the surface. Two samples AUB1010-6.63 m and AUB1010-8.25 m exhibit very high  $C_{poro,SO_4}$  values (~520 mmol/L PW), out of range of the other samples. After verification, these two values were due to the presence of gypsum that dissolved during sample leaching; consequently the  $C_{leached,SO_4}$  measured in these two samples cannot be considered as representative of the  $C_{poro,SO_4}$ , although  $C_{leached,SO_4}$  were correlated with solid/liquid ratios. In the lower part of the Tégulines Clay, the  $C_{poro,SO_4}$  deduced from leaching of samples conditioned in liquid nitrogen was lower than 10 mmol/L PW, whereas  $C_{poro,SO_4}$  deduced from leaching of samples conditioned in aluminum bags were systematically higher (9–30 mmol/L PW), confirming the importance of the sample conditioning [46, 47]. These values were not further discussed.

### 5.3. Exchangeable Fraction

**5.3.1. Cation Exchange Capacity and Distribution of Cations on the Clay Exchanger.** The CEC measured by colorimetry ( $CEC_{col}$ ) ranged between 10 and 24.9 meq/100  $g_{dry\ rock}$  with a mean value of  $15.0 \pm 3$  meq/100  $g_{dry\ rock}$ . The rare highest values were measured either in weathered samples near surface or near the interface with Greensands or in boreholes in which thickness of the Tégulines Clay was reduced due to erosion (AUB161 borehole). This CEC increase could be due (1) to a slight increase of the smectite component in the clay fraction and/or (2) to a slight contribution of iron hydroxides. Smectite component and iron hydroxides increased in weathered samples near surface, whereas smectite component only increased in samples near the interface with Greensands.

The  $CEC_{col}$  was almost similar to the sum of exchangeable cations ( $CEC_{\Sigma} = Ca + Mg + K + Na$ ) in weathered samples, indicating that CEC measurements were not perturbed by mineral dissolution, except the two samples containing gypsum (AUB1010-6.63 m and AUB1010-8.25 m). The  $CEC_{col}$  were systematically higher than the sum of exchangeable cations ( $CEC_{\Sigma} = Ca + Mg + K + Na$ ) in reduced samples. The  $NH_4^+$  contents measured in reduced samples from the AUB1010 borehole below 10 m (data not shown) were surprisingly high; this excess of  $NH_4^+$  corresponded to cobalt hexammine trichloride releasing  $NH_4^+$  in response to reduction of its Co(III) and could attest to the good preservation of the initial reduced state of the clay samples [48].

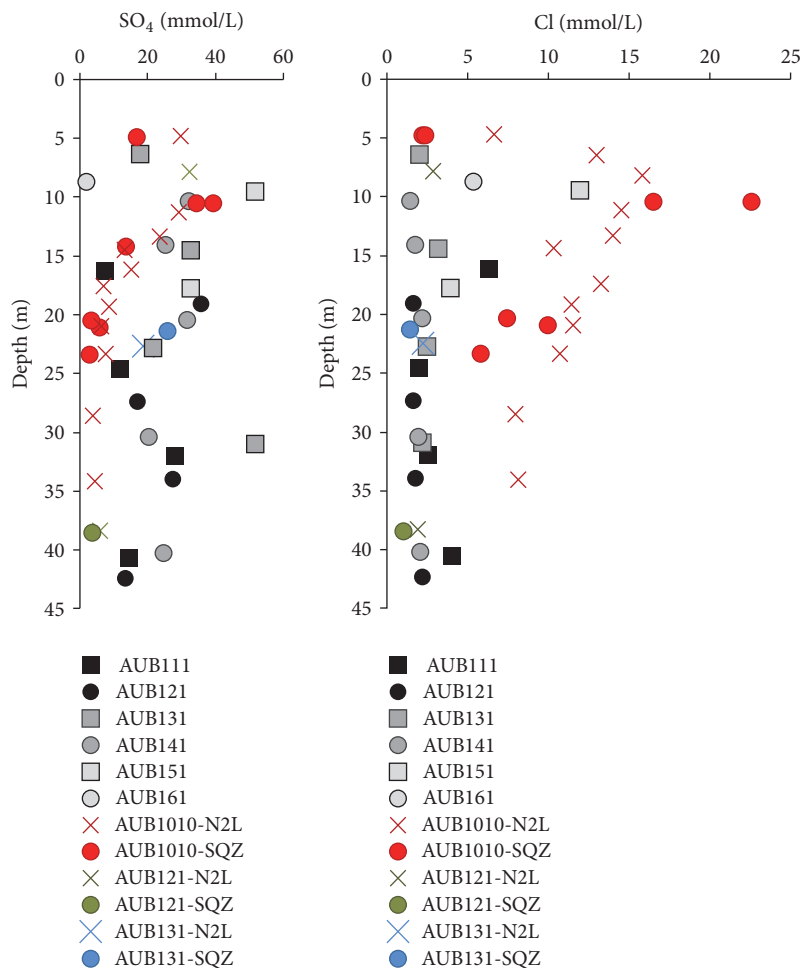


FIGURE 8: Chloride and sulfate concentrations of the AUB1010 borehole as a function of depth based on anion leaching data and directly measured on pore waters extracted by squeezing. Different symbols are used for data obtained on different boreholes. N2L indicates data obtained by leaching on samples preserved in liquid nitrogen, SQZ indicates data obtained on pore waters extracted by SQZ, the others correspond to data obtained by leaching on samples conditioned in aluminum bag.

Exchangeable cation concentrations were quite homogeneous through the different boreholes crosscutting the Tégulines Clay (Supplementary Appendix 2). Ca was the dominant adsorbed cation, followed by Mg, K, and Na. Toward the surface (<10 m), the CEC and the distribution of exchangeable cations were more heterogeneous. Some samples had high  $CEC_{col}$  values associated with higher cation concentrations. High anomalous Ca values were measured in the two samples containing gypsum (AUB1010-6.63 m and AUB1010-8.25 m).

**5.3.2. Exchangeable Strontium: Concentrations and  $^{87}Sr/^{86}Sr$  Ratios.** When coupled with Sr concentrations, Sr-isotope systematics can be used to investigate mixing of different groundwaters [49]. The  $^{87}Sr/^{86}Sr$  ratios of exchangeable strontium, considered as representative of  $^{87}Sr/^{86}Sr$  of present-day pore waters [50, 51], were measured in Tégulines Clay of the AUB1010 borehole. The exchangeable strontium contents decreased from the bottom of the Tégulines Clay toward the surface; this decrease could be due to dilution of marine-derived pore waters by surficial waters, but also

to slight precipitation of celestite. The  $^{87}Sr/^{86}Sr$  ratios of samples below 15 m ranged between 0.707416 and 0.707450, that is, slightly higher values than the signature of Cretaceous seawater [43]. When shallower (0–15 m),  $^{87}Sr/^{86}Sr$  ratios slightly increased toward the surface up to 0.708004. The slight enrichment in  $^{87}Sr$  could originate from the clay formation itself due to weathering processes of clay minerals but could be also due to support of external source such as meteoric waters [52], atmospheric deposition [53], anthropogenic sources [54], and/or mineral dissolution in surficial formations [49].

**5.4. Oxygen and Hydrogen Isotopes of Pore Waters.** The  $\delta^{18}O$  and  $\delta D$  of extracted pore waters ranged between  $-8.7$  and  $-5.9$ ‰ SMOW and between  $-61.5$  and  $-44.1$ ‰ SMOW, respectively, and are consistent with meteoric waters taking account of the uncertainty due to the analytical technique (Figure 9). The pore waters  $\delta^{18}O$  and  $\delta D$  of unoxidized samples (between 19.0 and 34.1 m) are close to Greensands waters (Bougligny). The pore waters  $\delta^{18}O$  and  $\delta D$  of samples in the weathered zone (between 4.8 and 13.4 m) are more

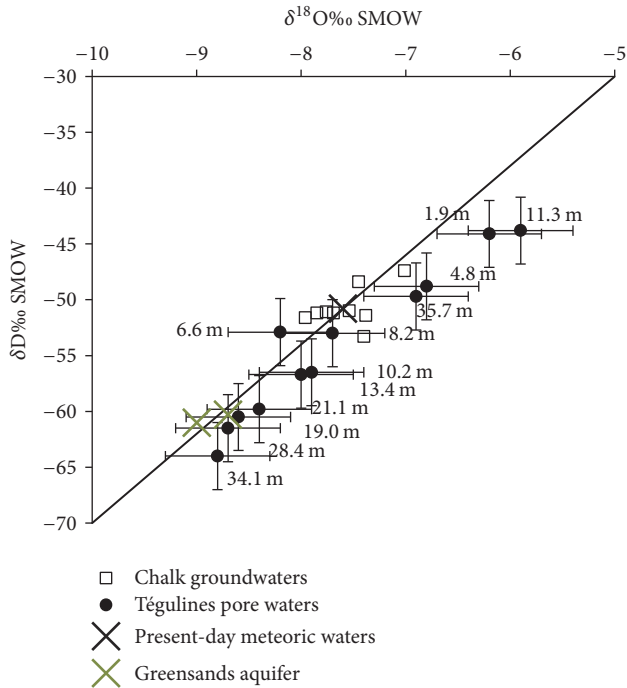


FIGURE 9:  $\delta^{18}\text{O}$ - $\delta\text{D}$  diagram in which the Tégulines waters, the meteoric water line (MLW), local present-day meteoric waters [29], and Greensand aquifer (Bougligny) [30] are reported.

heterogeneous and evolve to local present-day meteoric waters. The pore waters  $\delta^{18}\text{O}$  and  $\delta\text{D}$  of sample at the bottom of the Tégulines Clay at interface with Greensands (35.7 m) are also close to present-day pore waters, suggesting local support of fresh meteoric waters in the Greensands aquifer. The values systematically lower than the meteoric water line and the few values clearly different from the others by their significant  $^{18}\text{O}$  and D enrichment (for example, sample 11.32 m) might be interpreted in terms of climate conditions (rather humid conditions) and evaporation processes. These data need to be validated.

**6. Discussion**

**6.1. Oxidation Profile.** Redox fronts based on mineralogical (redox-sensitive minerals) and geochemical (redox-sensitive elements such as Fe, Ce, and U) investigations in fractures were highly studied in granitic environments [12, 14, 55] and in some types of sedimentary rocks [12, 56] but less in clay-rocks [13]. For the Tégulines Clay, we favored general macroscopic and mineralogical observations of the clay rather than a targeted study of fractures, as fractures were rare and difficult to identify due to the plasticity of the rock.

We were able to collect much “macroscopic” evidence of weathering processes, including oxidation. First, the color changed from ochrous to greenish grey below 5 m. Second, gypsum and iron hydroxides were macroscopically observed down to 9-10 m as in situ replacement of pyrite and iron hydroxides were seen to fill a vertical fracture and planes subparallel to the bedding. Third, we saw a change of consistency from a plastic to a nonplastic clay below ~20 m.

Combined macroscopic and microscopic observations and chemical, isotopic, and petrophysical data rather indicate that oxidation of the clay formation is characterized more by progressive reactions than by a sharp redox reaction front. In Tégulines Clay, extension of oxidation reactions can be described according to various related effects on the rock properties as observed on the well-preserved reduced clay at ~21 m to the oxidized clay at surface (Figure 10).

Deeper than 21 m, Tégulines Clay samples were dark green, hard, and reduced. The general texture of the Tégulines Clay and the low burial depth (about 300–600 m) indicated low diagenetic process intensity without extensive precipitation of minerals (such as micritic carbonates). However observations of septarian veining in phosphate nodules attested to compaction processes. The low diagenesis process intensity resulted in larger pore diameters and porosity ( $28 \pm 3\%$ ) in comparison to clay-rock strongly influenced by chemical compaction, such as the Callovo-Oxfordian or Opalinus clay formations for instance [57–59]. Unweathered Tégulines Clay consisted of more than 75% of detrital minerals including quartz, K-feldspar, kaolinite, chlorite, illite-smectite and chlorite-smectite mixed layers, detrital calcite and phosphate bioclasts, and intratracces of goethite and magnetite. Detrital minerals did not provide evidence of dissolution features. Phosphate bioclasts were often enclosed in nodules of diagenetic phosphate (francolite), indicating they were not stable, whereas calcite bioclasts (shells, tests) were relatively well preserved. Diagenetic minerals consisted of glauconite ( $8 \pm 6\%$ ) with variable amounts of calcite and minor dolomite, siderite, pyrite, and phosphates. All these diagenetic minerals are commonly formed at early stage of diagenesis in the bacterial sulfate reduction (BSR) zones of marine clay formations that evolved in reducing conditions [7, 8]. The microsparite and celestite, contemporaneous of the compaction, filled the residual porosity. The bulk  $\text{Fe}^{2+}/(\text{Fe}^{2+} + \text{Fe}^{3+})$  ratio of ~0.8 characterized the reduced state of the clay-rocks. The dark green color and the chemical composition of glauconite aggregates are consistent with highly evolved Fe-poor glauconite formed in a context of high sedimentation rate according to [20].

From ~21 m up to ~10-11 m, Tégulines Clay samples remained dark green and reduced and became plastic. The bulk  $\text{Fe}^{2+}/(\text{Fe}^{2+} + \text{Fe}^{3+})$  ratio remained close to ~0.7–0.8 attesting of the stability of the reduced state of the clay-rocks. The oxidation degree was low and mainly detectable by the change of consistency due to the progressive increase of water content and porosity ( $30 \pm 3\%$ ) toward shallower depths, by slight increase of goethite content, disappearance of magnetite, and observations under the microscope of some yellowish-greenish rounded aggregates of glauconite (transmitted light).

From ~10-11 m up to 5 m, Tégulines Clay samples were green and plastic. Plasticity is always correlated with the increase of water content and porosity ( $33 \pm 4\%$ ) toward shallower depths. The degree of oxidation was high, characterized by observations of some yellowish-brownish rounded aggregates of glauconite, substantial oxidation of pyrite into gypsum and iron hydroxides (major goethite), total oxidation

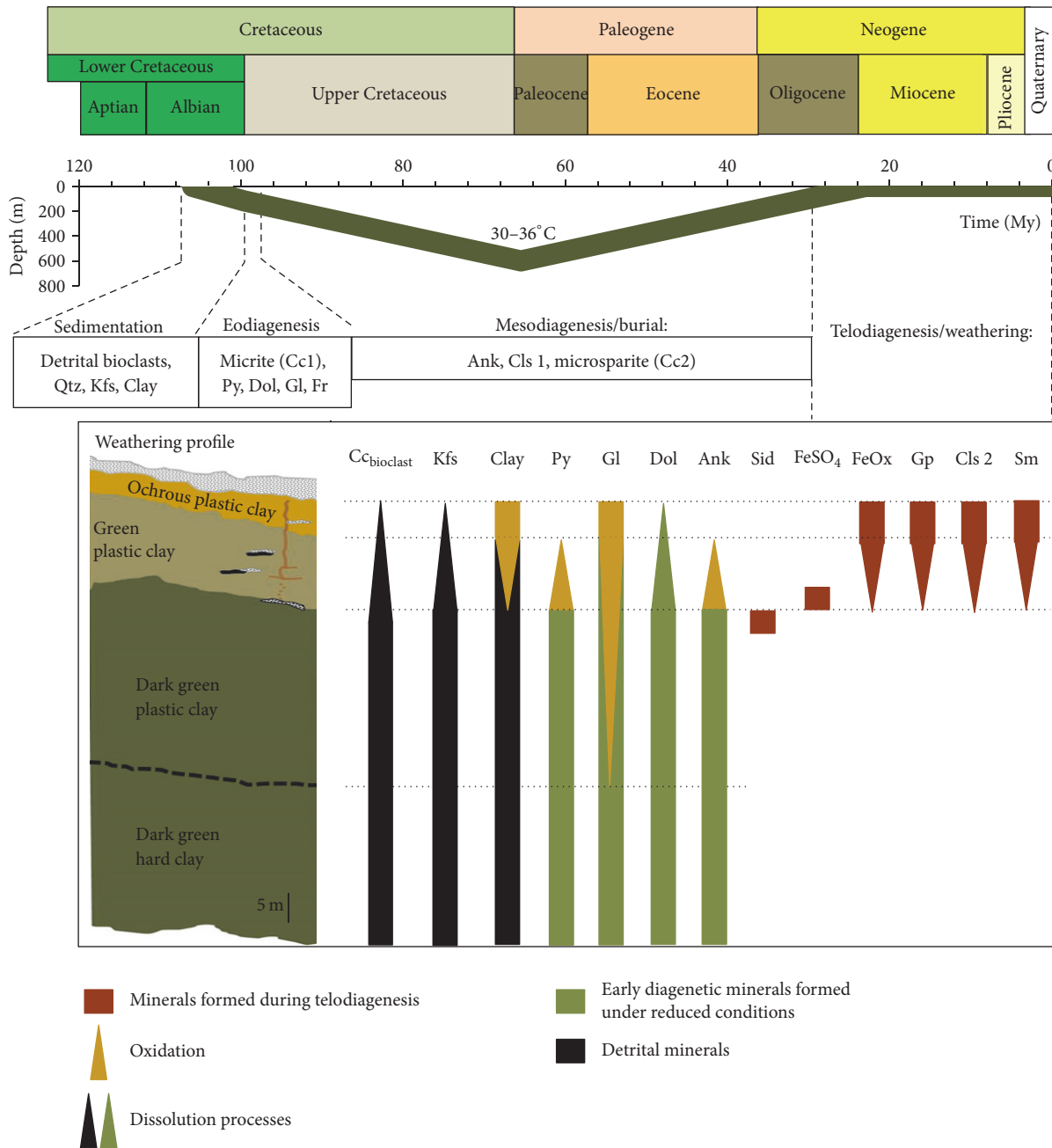


FIGURE 10: Burial curve proposed for the Tégulines Clay and diagenetic mineral sequence. The mineral sequence including processes of dissolution, oxidation, and precipitation is detailed in function of depth for the telodiagenesis. Ank, ankerite; Cc bioclast, calcite from detrital bioclasts; Clay, undifferentiated detrital clay matrix including kaolinite, illite-smectite mixed layer minerals, chlorite, illite/mica; Cls, celestite; Dol, dolomite; FeOx, iron oxide-hydroxides; fr, francolite; Gl, glauconite; Gp, gypsum; Kfs, potassic feldspar; Py, pyrite; Qtz, quartz; Sid, siderite; Sm, smectite.

of ankerite into iron hydroxides and partial dissolution of K-feldspar and calcite. The high oxidation is marked by the significant change of the  $Fe^{2+}/(Fe^{2+} + Fe^{3+})$  ratio from 0.8 to ~0.2.

From 5 m deep and up to the surface, the Tégulines Clay color changed from green to ochrous and was highly plastic. The porosity attained value of  $35 \pm 4\%$ . Pyrite was entirely oxidized into gypsum and iron hydroxides (goethite ~2%). The  $Fe^{2+}/(Fe^{2+} + Fe^{3+})$  ratio was closed to 0–0.1.

Above 9–11 m, the plasticity and porosity changes were the most developed and could be associated with several processes: increase of water interacting with clay particles, nonswelling clay minerals transforming into smectite, minerals dissolving, formation of expansive minerals, and rock physically decompacting due to progressive decrease in the lithostatic pressure. Among them, the pyrite oxidation is the major process involved in the deterioration of clay-rock, due to the formation of expansive phases such as gypsum and

TABLE 3: Distribution and iron speciation in iron-bearing minerals of well-preserved reduced Tégulines Clay and weathered Tégulines Clay.

| Minerals                    | Mineral content (wt%) | Fe <sup>2+</sup> /total Fe ratio | Total Fe mmole/100 g of rock | Total Fe <sup>2+</sup> mmole/100 g of rock | Fe carried by the mineral/total Fe |
|-----------------------------|-----------------------|----------------------------------|------------------------------|--|------------------------------------|
| Reduced Tégulines Clay      |                       |                                  |                              |  |                                    |
| Pyrite                      | 0.9                   | 1.0                              | 7.5                          | 7.5  | 10.4                               |
| Siderite                    | 0.5                   | 1.0                              | 3.1                          | 3.1  | 4.3                                |
| Goethite                    | 0.7                   | 0.0                              | 7.9                          | 0.0  | 11.0                               |
| Glaucosite                  | 9.0                   | 0.8                              | 25.0                         | 20.0                                       | 34.8                               |
| Clay (Ill + Ill-Sm, Sm-Chl) | 28.0                  | 0.8                              | 28.4                         | 23.7                                       | 39.5                               |
| <i>Bulk rock</i>            |                       | 0.8                              | 71.9                         | 54.3                                       | 100.0                              |
| Oxidized Tégulines Clay     |                       |                                  |                              |  |                                    |
| Pyrite                      | 0.1                   | 1.0                              | 0.8                          | 0.8  | 1.2                                |
| Siderite                    | 0.5                   | 1.0                              | 3.1                          | 3.1  | 4.3                                |
| Goethite                    | 2.0                   | 0.0                              | 20.8                         | 0.0  | 28.9                               |
| Glaucosite                  | 9.0                   | 0.2                              | 18.8                         | 3.8  | 26.1                               |
| Clay (Ill + Ill-Sm, Sm-Chl) | 28.0                  | 0.2                              | 28.4                         | 5.7  | 39.5                               |
| <i>Bulk rock</i>            |                       | 0.2                              | 71.9                         | 13.4                                       | 100.0                              |

goethite [60]. No extensive clay minerals to smectite transformations were evidenced by X-ray diffraction, CEC measurements, and strontium isotopes of exchangeable strontium. The depth of ~9–11 m is the transition between the highly reactive clay and the slightly oxidized clay. This transition could be also interpreted as the maximum depth of the structural modifications (vertical fracture) of the Tégulines Clay due to weathering processes (e.g., climate changes, saturation/desaturation cycles). Structural modifications might have favored infiltration of oxidizing meteoric fluids at depth and the network of siderite in the AUB1010–11.32 m sample might have been an exceptional example of the reactivity of reduced Tégulines Clay with surficial fluids enriched in iron and in dissolved bicarbonates diffusing through these vertical fractures. The process of siderite precipitation and extension of the vertical fractures need to be validated by further investigations.

A distribution of iron (Fe<sup>2+</sup>/(Fe<sup>2+</sup> + Fe<sup>3+</sup>)) among the mineral phases of the Tégulines Clay was approximatively estimated for the unweathered (reduced) Tégulines Clay and weathered clay using a mass balance approach based on bulk iron contents, Fe<sup>2+</sup>/(Fe<sup>2+</sup> + Fe<sup>3+</sup>) ratios, mineral contents, and mineral chemistry (Table 3). Due to its low content compared to other Fe<sup>2+</sup>-bearing phases, ankerite was not considered in the calculations. Siderite oxidation was assumed to be negligible compared to pyrite oxidation [61]. Glaucosite was assumed to be constant through the Tégulines Clay, although it slightly decreased. The oxidation of other Fe-bearing clay minerals was assumed in a first approximation to be negligible compared to glaucosite oxidation, although the presence of iron hydroxides was detected in rare large flakes of chlorite, for example. Oxidation essentially affected pyrite (~90%), glaucosite (not determined), and magnetite (100%) and mobilized about ~7 mmoles of Fe per 100 g of rock, that is, ~9–10% of the total iron. This liberated iron

essentially precipitated essentially in situ in the form of goethite, according to magnetic remanence measurements. Oxidation of rare pyrite-rich layers can mobilize more iron and sulfur.

6.2. *Consequence of Weathering on Pore Water Chemistry.* Present-day pore waters have strongly evolved from the Albian seawater during early diagenesis, compaction, burial, and uplift due to erosion up to outcrop. Their global history is complex and must consider the past influences of external waters coming from surrounding rocks (Overlying Cretaceous chalk and underlying Greensands), the percolation of meteoric waters, and the water/rock interactions. The previous rock characterization of this study highlighted several zones of mineral reaction due to weathering in the upper part of the Tégulines Clay that must be taken into account to better understand the present-day chemical variations in the pore waters.

The  $\delta^{18}\text{O}$  and  $\delta\text{D}$  of present-day Tégulines pore waters show that surficial waters have diffused through the clay formation (Figure 11). In the lower part of the Tégulines Clay (below 20 m in the AUB1010 borehole but not close to the Greensands), early reduced diagenetic conditions are preserved and all the early mineralogy remain stable. Consequently pore waters of this zone can be considered as the most representative of diagenetic pore waters that have been little modified by weathering (Figure 11). They are characterized by low  $C_{\text{poro,Cl}}$  (<10 mmol/L) and  $C_{\text{poro,SO}_4}$  (<10 mmol/L), low ionic strengths, and a cation exchange population dominated by Ca and Mg due to exchange preference for divalent cations over monovalent cations at low ionic strength [62].  $^{87}\text{Sr}/^{86}\text{Sr}$  ratios close to Cretaceous seawater combined with exchangeable strontium contents strongly confirm dilution by meteoric fluids but low water/clay interactions concerning strontium. By comparison, the pore waters in the upper



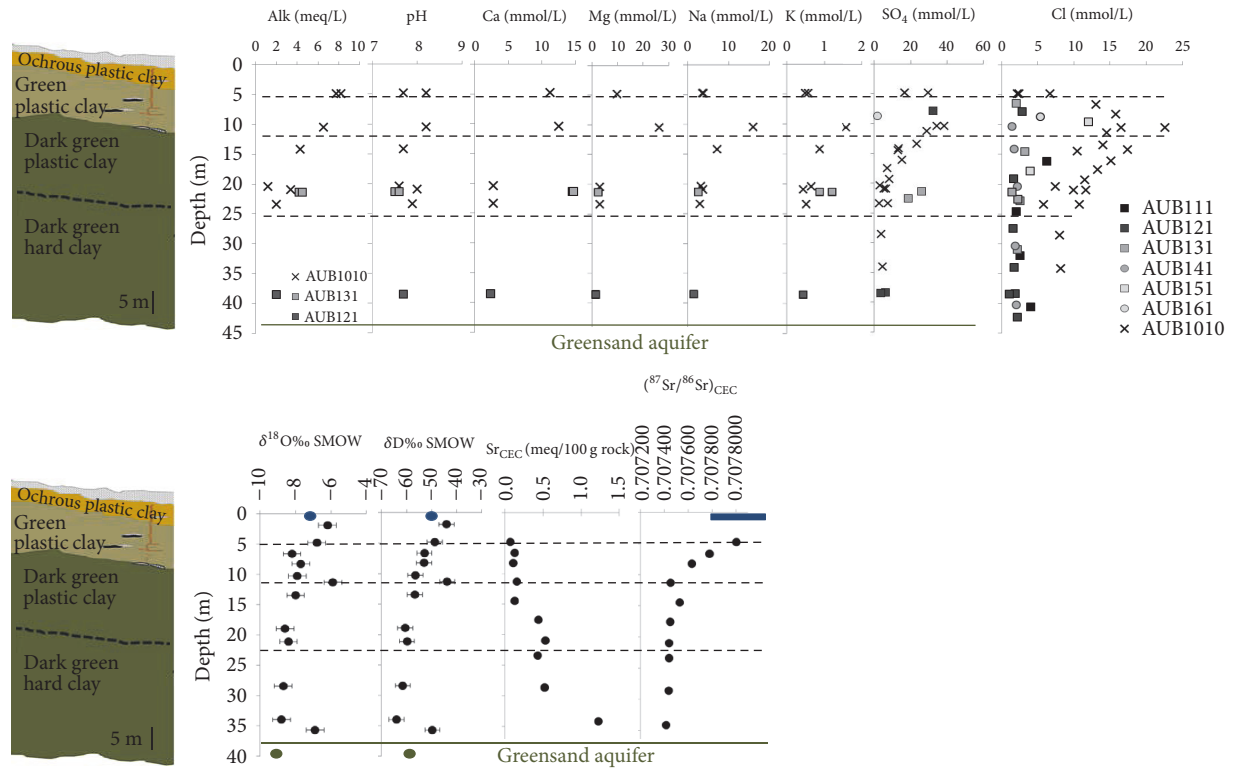


FIGURE 11: Chemical characterization of pore waters and weathering profile. (a) Chloride and sulfate concentrations of pore waters as a function of depth based on anion leaching data and directly measured on pore waters extracted by squeezing (all boreholes). (b) Profiles of alkalinity, pH cation (squeezing), and anion concentrations (squeezing and leaching data) in pore waters as a function of depth. (c) Profiles of  $\delta^{18}\text{O}$  and  $\delta\text{D}$  of pore waters, contents, and  $^{87}\text{Sr}/^{86}\text{Sr}$  of exchangeable strontium through the Tégulines Clay (AUB1010 borehole only). Blue points and lines correspond to meteoric waters and green points to Greensand aquifer.

part of the layer (above 20 m in the AUB1010 borehole) are characterized by heterogeneous and higher  $C_{\text{poro,Cl}}$  and  $C_{\text{poro,SO}_4}$ , higher alkalinity, higher ionic strengths (up to 175 mmol/L), and a modified cation exchange population. The chemical variations in pore waters toward the surface essentially result from mineral changes due to oxidation. Observations combined with high  $^{87}\text{Sr}/^{86}\text{Sr}$  ratios suggest instead that  $^{87}\text{Sr}$  support in pore waters is mainly due to external support but also to dissolution/alteration of Sr-bearing minerals such as glauconite and K-feldspar. The change of sulfur (S(0) and S(-2) to S(+6) and iron (Fe(2) to Fe(3)) speciation toward the surface is characterized by the partial to total dissolution of Fe<sup>2+</sup> bearing minerals (pyrite, ankerite, siderite, and magnetite). The consequences of pyrite oxidation following the reaction equation  $\text{FeS}_2 + 7/2 \text{O}_2 + \text{H}_2\text{O} \rightarrow \text{Fe}^{2+} + 2\text{SO}_4^{2-} + 2 \text{H}^+$  are the most important [60]. The reaction liberates sulfates, iron ions, and protons. According to mineral characterization, pyrite oxidation in 100 g of Tégulines Clay mobilizes about 7 mmoles of Fe, 14 mmoles of sulfates, and 14 mmoles of H<sup>+</sup>.

Sulfates partially precipitate as gypsum and minor celestite. Iron precipitates as iron hydroxides, dominantly goethite identified by magnetic remanence. Liberation of protons decreases the pH and by reactivity dissolves the

carbonates to produce CO<sub>2</sub>, with the liberation of calcium and possibly magnesium.

The highest variations of pore water chemistry were observed in the 5–10 m zone which is the most reactive (Figure 11). Above 5 m, pore waters are diluted by infiltrating meteoric waters and controlled by the mineral assemblage formed in oxidized conditions. Below 10–11 m, pore waters result from the slow diffusion of pore waters descending from the 5–10 m reactive zone. At this stage of the work, mineral changes may explain high sulfate concentrations in pore waters, the increasing alkalinity, and the heterogeneities of Ca and Mg of the clay exchanger due to partial dissolution of carbonates (e.g., calcite, dolomite, and ankerite). The varying Cl concentrations in pore waters remain unexplained. They could be due to external support and/or the dissolution of Cl-bearing phases that have not been identified.

### 6.3. Reactivity of Tégulines Clay to Weathering: Key Solute Transport Parameters.

Understanding the chemical composition of pore waters and its regulation is important for predicting contaminant mobility in rock formations. The speciation, solubility, and retention properties of contaminants are strongly influenced by the pore water chemistry.

Spatial evolution in pore water chemistry in Tégulines Clay depends on the present-day hydrogeological context,

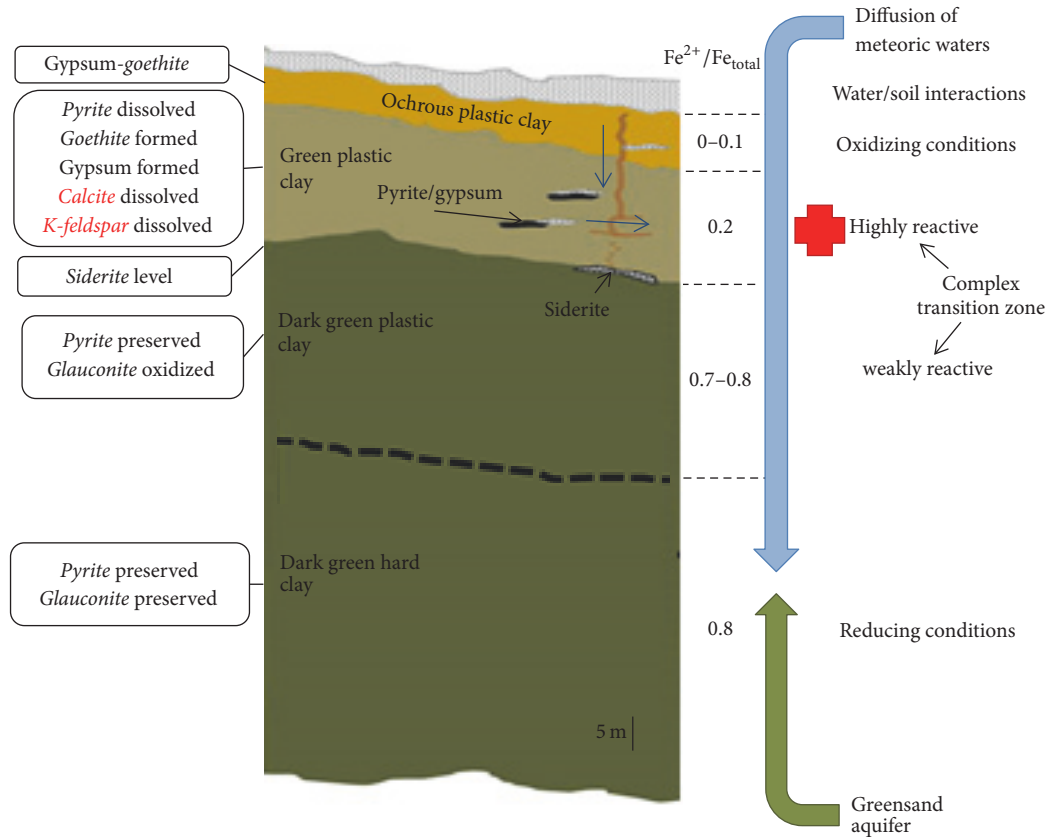


FIGURE 12: Sketch model of the near-surface redox front in the Tégulines Clay. The different fields are based on color, redox- (in black and bold) and pH-sensitive (in red) minerals, iron which is a redox-sensitive element and plasticity change.

topography, erosion, and weathering processes. Even interactions between rock and diffusive surficial oxidizing waters remain limited, so the sorption capacity of the clay minerals is preserved. The effect of oxidation on the pore water chemistry can impact the speciation of redox-sensitive contaminants (uranium for instance), so further investigations are required in this field.

Chloride concentrations acquired both by aqueous leaching and by squeezing reveal the low anion exclusion, phenomenon classically described in other clay-rock formations (Callovo-Oxfordian mudstones, Opalinus clay) [63]. The low anion exclusion in the Tégulines Clay can be explained by the geometry of the pore space (and limited diagenetic processes) characterized by pore diameters mainly higher than 30–50 nm. The effect of electrostatic interactions on solute transport appears to be relatively restricted in the Tégulines Clay, potentially easing the undersetting of contaminant transport.

Beyond the uncertainties generated by oxidation on contaminant mobility, weathering-related effects can also help us to better understand and quantify the transport of solute at the scale of the rock formation. Natural tracers ( $\delta^{18}\text{O}$  and  $\delta\text{D}$  of pore waters,  $^{87}\text{Sr}/^{86}\text{Sr}$  ratios of exchangeable strontium) highlighted evidence of diffusion of meteoric waters through Tégulines Clay, involving the dilution of pristine marine-derived waters. Coupled reactive transport modelling is now required to properly interpret the chemistry

of the pore waters and extract quantitative parameters on solute transport, if possible.

## 7. Conclusions

Combined macroscopic and microscopic observations and geochemical and petrophysical data allow us to propose a first sketch model of the redox changes in the Tégulines Clay and their consequences on the clay pore water chemistry (Figure 12). This first sketch model is based on the major iron-bearing redox-sensitive minerals such as pyrite, glauconite, siderite, and iron hydroxides, on the valence of iron and on the petrophysical properties. Other redox proxies such as Mn, Ce, and U [12, 13], the partial pressure of  $\text{CO}_2$  which is a classic parameter used to control pH or alkalinity in clay-rocks [64–66], trace element behavior, and isotopes sensitive to clay weathering such as Li and Sr are currently investigated.

This first sketch model shows that oxidation of Tégulines Clay is characterized more by progressive reactions than by a sharp redox reaction front:

(1) The extension of oxidation reactions can be described as observed on the well-preserved reduced clay at ~20 m to the oxidized clay at surface. This zone corresponds to the transition between a nonplastic to a plastic rock and to glauconite oxidation.

(2) The thickness of the entirely oxidized clay is limited to the first 2–3 meters.

(3) The following 7-8 m corresponds to a highly reactive clay influenced essentially by pyrite oxidation and affected by fracturation.

(4) Siderite network might represent the reaction front between oxidizing meteoric fluids and the reduced clay between a highly reactive zone and reduced clay.

The present-day Tégulines pore water chemistry is heterogeneous and results from the dilution of modified marine waters by oxidizing meteoric fluids diffusing through the clay formation and by water-rock interactions and more specifically by the pyrite oxidation in the highly reactive transition zone.

All these data constitute a set of parameters that should allow us to constrain vertical solute reactive transport modelling through the Tégulines Clay firstly at the scale of a borehole and secondly at the scale of the studied area taking into account erosion and the hydrological network that has been in place for 23 Ma.

## Conflicts of Interest

The authors declare that they have no conflicts of interest.

## Acknowledgments

This study was supported financially by the French National Radioactive Waste Management Agency (ANDRA) and the French Geological Survey (BRGM). This is IGCP contribution 3909. The authors acknowledge M. Alleki, E. Découchon, C. Fauchet, E. Huret, and S. Touzelet for their technical assistance and S. Grangeon and N. Maubec for XRD. They are very grateful to Dr. Karen M. Tkaczyk who improved the English of this article.

## Supplementary Materials

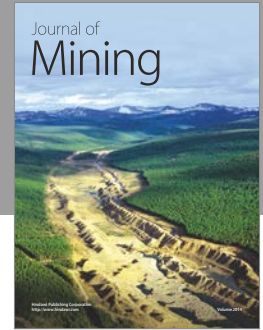
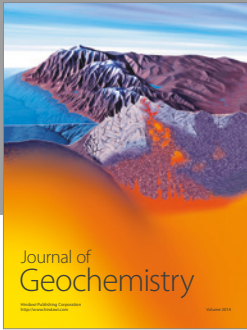
Supplementary Appendix 1 gives the detailed description of the different analytical techniques. Supplementary Appendix 2 is an excel file including mineralogy, bulk chemistry (major elements), CEC data, leaching data, squeezing data, stable isotope data, and porosity. Supplementary Appendix 3 represents the X-ray diffraction pattern of a phosphate nodule. Supplementary Appendix 4 gives the detailed data of magnetic remanence. (*Supplementary Materials*)

## References

- [1] D. E. Desaulniers, J. A. Cherry, and P. Fritz, "Origin, age and movement of pore water in argillaceous Quaternary deposits at four sites in southwestern Ontario," *Journal of Hydrology*, vol. 50, no. C, pp. 231–257, 1981.
- [2] V. H. Remenda, J. A. Cherry, and T. W. D. Edwards, "Isotopic composition of old ground water from Lake Agassiz: Implications for late Pleistocene climate," *Science*, vol. 266, no. 5193, pp. 1975–1978, 1994.
- [3] M. J. Hendry, C. J. Kelln, L. I. Wassenaar, and J. Shaw, "Characterizing the hydrogeology of a complex clay-rich aquitard system using detailed vertical profiles of the stable isotopes of water," *Journal of Hydrology*, vol. 293, no. 1-4, pp. 47–56, 2004.
- [4] M. Mazurek, P. Alt-Epping, A. Bath, T. Gimmi, and H. N. Waber, *Natural Tracer Profiles Across Argillaceous Formations-The CLAYTRAC Project*, P. Organ. for Econ. Coop. and Dev. Nucl. Energy Agency, 2009.
- [5] M. Mazurek, P. Alt-Epping, A. Bath et al., "Natural tracer profiles across argillaceous formations," *Applied Geochemistry*, vol. 26, no. 7, pp. 1035–1064, 2011.
- [6] M. J. Hendry and L. I. Wassenaar, "Controls on the distribution of major ions in pore waters of a thick surficial aquitard," *Water Resources Research*, vol. 36, no. 2, pp. 503–513, 2000.
- [7] C. Lerouge, S. Grangeon, E. C. Gaucher et al., "Mineralogical and isotopic record of biotic and abiotic diagenesis of the Callovian-Oxfordian clayey formation of Bure (France)," *Geochimica et Cosmochimica Acta*, vol. 75, no. 10, pp. 2633–2663, 2011.
- [8] C. Lerouge, S. Grangeon, F. Claret et al., "Mineralogical and isotopic record of diagenesis from the Opalinus Clay formation at Benken, Switzerland: Implications for the modeling of pore-water chemistry in a clay formation," *Clays and Clay Minerals*, vol. 62, no. 4, pp. 286–312, 2014.
- [9] R. E. Gerber, J. I. Joseph, and K. W. F. Howard, "Evaluation of heterogeneity and field-scale groundwater flow regime in a leaky till aquitard," *Hydrogeology Journal*, vol. 9, no. 1, pp. 60–78, 2001.
- [10] L. D. McKay and J. Fredericia, "Distribution, origin, and hydraulic influence of fractures in a clay-rich glacial deposit," *Canadian Geotechnical Journal*, vol. 32, no. 6, pp. 957–975, 1995.
- [11] M. J. Hendry, J. A. Cherry, and E. I. Wallick, "Origin and Distribution of Sulfate in a Fractured Till in Southern Alberta, Canada," *Water Resources Research*, vol. 22, no. 1, pp. 45–61, 1986.
- [12] H. Drake, E.-L. Tullborg, and A. B. MacKenzie, "Detecting the near-surface redox front in crystalline bedrock using fracture mineral distribution, geochemistry and U-series disequilibrium," *Applied Geochemistry*, vol. 24, no. 5, pp. 1023–1039, 2009.
- [13] M. Mazurek, W. R. Alexander, and A. B. Mackenzie, "Contaminant retardation in fractured shales: Matrix diffusion and redox front entrapment," *Journal of Contaminant Hydrology*, vol. 21, no. 1-4, pp. 71–84, 1996.
- [14] K. Dideriksen, B. C. Christiansen, J. A. Baker et al., "Fe-oxide fracture fillings as a palæo-redox indicator: Structure, crystal form and Fe isotope composition," *Chemical Geology*, vol. 244, no. 1-2, pp. 330–343, 2007.
- [15] C. Yu, H. Drake, F. A. Mathurin, and M. E. Åström, "Cerium sequestration and accumulation in fractured crystalline bedrock: The role of Mn-Fe (hydr-)oxides and clay minerals," *Geochimica et Cosmochimica Acta*, vol. 199, pp. 370–389, 2017.
- [16] R. Tostevin, G. A. Shields, G. M. Tarbuck, T. He, M. O. Clarkson, and R. A. Wood, "Effective use of cerium anomalies as a redox proxy in carbonate-dominated marine settings," *Chemical Geology*, vol. 438, pp. 146–162, 2016.
- [17] L. D. McKay, J. A. Cherry, and R. W. Gillham, "Field experiments in a fractured clay till: 1. Hydraulic conductivity and fracture aperture," *Water Resources Research*, vol. 29, no. 4, pp. 1149–1162, 1993.
- [18] J. Gonçalves, M. Pagel, S. Violette, F. Guillocheau, and C. Robin, "Fluid inclusions as constraints in a three-dimensional hydrothermo-mechanical model of the Paris basin, France," *Basin Research*, vol. 22, no. 5, pp. 699–716, 2010.

- [19] A. Meunier and B. Velde, "Solid solutions in I/S mixed-layer minerals and illite," *American Mineralogist*, vol. 74, no. 9-10, pp. 1106-1112, 1989.
- [20] A. Baldernann, M. Dietzel, V. Mavromatis, F. Mittermayr, L. N. Warr, and K. Wemmer, "The role of Fe on the formation and diagenesis of interstratified glauconite-smectite and illite-smectite: A case study of Lower Cretaceous shallow-water carbonates," *Chemical Geology*, vol. 453, pp. 21-34, 2017.
- [21] A. Meunier and A. El Albani, "The glauconite-Fe-illite-Fe-smectite problem: A critical review," *Terra Nova*, vol. 19, no. 2, pp. 95-104, 2007.
- [22] S.-T. Kim and J. R. O'Neil, "Equilibrium and nonequilibrium oxygen isotope effects in synthetic carbonates," *Geochimica et Cosmochimica Acta*, vol. 61, no. 16, pp. 3461-3475, 1997.
- [23] M. Schmidt, S. Xeflide, R. Botz, and S. Mann, "Oxygen isotope fractionation during synthesis of CaMg-carbonate and implications for sedimentary dolomite formation," *Geochimica et Cosmochimica Acta*, vol. 69, no. 19, pp. 4665-4674, 2005.
- [24] W. W. Carothers, L. H. Adami, and R. J. Rosenbauer, "Experimental oxygen isotope fractionation between siderite-water and phosphoric acid liberated CO<sub>2</sub>-siderite," *Geochimica et Cosmochimica Acta*, vol. 52, no. 10, pp. 2445-2450, 1988.
- [25] F. Amédéo, B. Matrimon, F. Magniez-Jannin, and R. Touch, "La limite Albien inférieur-Albien moyen dans l'Albien type de l'Aube (France): ammonites, foraminifères, séquences," *Revue de Paléobiologie*, vol. 33, no. 1, pp. 159-279, 2014.
- [26] F. Amédéo and P. Destombes, "Présence du genre *Knemicerias* (Ammonoidea, Engonoceratidae) dans l'Albien moyen de l'Aube (France)," *Bulletin d'Information des Géologues du Bassin de Paris*, vol. 21, no. 4, pp. 21-25, 1984.
- [27] B. Bomou, J.-F. Deconinck, E. Pucéat, F. Amédéo, M. M. Joachimski, and F. Quillévéré, "Isotopic seawater temperatures in the Albian Gault Clay of the Boulonnais (Paris Basin): palaeoenvironmental implications," *Proceedings of the Geologists' Association*, vol. 127, no. 6, pp. 699-711, 2016.
- [28] F. Amédéo, F. Magniez-Jannin, C. Collete, and C. Fricot, "L'Albien-type de l'Aube, France: Une révision Nécessaire - New data on the Albian Stratotype (Aube, France)," *Géologie de la France*, vol. 2, pp. 25-42, 1995.
- [29] R. Millot, E. Petelet-Giraud, C. Guerrot, and P. Négrel, "Multi-isotopic composition ( $\delta^{7}\text{Li}$ - $\delta^{11}\text{B}$ - $\delta^{\text{D}}$ - $\delta^{18}\text{O}$ ) of rainwaters in France: Origin and spatio-temporal characterization," *Applied Geochemistry*, vol. 25, no. 10, pp. 1510-1524, 2010.
- [30] P. Humez, "Traçage des intrusions de CO<sub>2</sub> dans les aquifères d'eau douce par les méthodes multi-isotopiques," in *ENMP*, 2012.
- [31] R. I. Knight, "Phosphates and phosphogenesis in the Gault Clay (Albian) of the Anglo-Paris Basin," *Cretaceous Research*, vol. 20, no. 5, pp. 507-521, 1999.
- [32] G. Breton, "The gault of Perthois : burrows, phosphates and small droppings," *Bulletin de l'Association Géologique Auloise*, vol. 31, pp. 3-66, 2011.
- [33] E. Lasseur, "La Craie du Bassin de Paris (Cénomaniens-Campaniens, Crétacé supérieur)," in *Sédimentologie de faciès, stratigraphie séquentielle et géométrie 3D*, p. 423, Université de Rennes, 2007.
- [34] J. Le Roux and D. Harmand, "Origin of the hydrographic network in the Eastern Paris Basin and its border massifs. Hypothesis, structural, morphologic and hydrographic consequences," *Géologie de la France*, vol. 1, pp. 105-110, 2003.
- [35] F. Guillocheau, C. Robin, P. Allemand et al., "Meso-Cenozoic geodynamic evolution of the Paris Basin: 3D stratigraphic constraints," *Geodinamica Acta*, vol. 13, no. 4, pp. 189-245, 2000.
- [36] C. Mégnien and F. Hanot, *Programme Craie 700: deux forages scientifiques profonds pour étudier les phénomènes diagénétiques de grande ampleur dans la craie du Bassin de Paris*, vol. 37 of *Bull. Inf. Geol. Bass. Paris*, C.H. Mégnien, 2000.
- [37] T. Blaise, J. Barbarand, M. Kars et al., "Reconstruction of low temperature (<100°C) burial in sedimentary basins: A comparison of geothermometer in the intracontinental Paris Basin," *Marine and Petroleum Geology*, vol. 53, pp. 71-87, 2014.
- [38] J. Barbarand, F. Quesnel, and M. Pagel, "Lower Paleogene denudation of Upper Cretaceous cover of the Morvan Massif and southeastern Paris Basin (France) revealed by AFT thermochronology and constrained by stratigraphy and paleosurfaces," *Tectonophysics*, vol. 608, pp. 1310-1327, 2013.
- [39] J. Gonçalves, S. Violette, C. Robin, D. Bruel, F. Guillocheau, and E. Ledoux, "Combining a compaction model with a facies model to reproduce permeability fields at the regional scale," *Physics and Chemistry of the Earth*, vol. 29, no. 1, pp. 17-24, 2004.
- [40] C. Ménétrier, M. Élie, L. Martinez et al., "Estimation of the maximum burial palaeotemperature for Toarcian and Callovian-Oxfordian samples in the central part of the Paris Basin using organic markers," *Comptes Rendus - Geoscience*, vol. 337, no. 15, pp. 1323-1330, 2005.
- [41] J. D. Schuffert, M. Kastner, G. Emanuele, and R. A. Jahnke, "Carbonate-ion substitution in francolite: A new equation," *Geochimica et Cosmochimica Acta*, vol. 54, no. 8, pp. 2323-2328, 1990.
- [42] Y. Guyodo, T. M. LaPara, A. J. Anschutz et al., "Rock magnetic, chemical and bacterial community analysis of a modern soil from Nebraska," *Earth and Planetary Science Letters*, vol. 251, no. 1-2, pp. 168-178, 2006.
- [43] C. E. Jones, H. C. Jenkyns, A. L. Coe, and H. P. Stephen, "Strontium isotopic variations in Jurassic and Cretaceous seawater," *Geochimica et Cosmochimica Acta*, vol. 58, no. 14, pp. 3061-3074, 1994.
- [44] T. J. Bralower and H. R. Thierstein, "Low productivity and slow deep-water circulation in mid-Cretaceous oceans," *Geology*, vol. 12, no. 10, pp. 614-618, 1984.
- [45] F. J. Pearson, "What is the porosity of a mudrock?" *Journal of the Geological Society*, vol. 158, pp. 9-21, 1999.
- [46] É. C. Gaucher, P. Blanc, F. Bardot et al., "Modelling the porewater chemistry of the Callovian-Oxfordian formation at a regional scale," *Comptes Rendus - Geoscience*, vol. 338, no. 12-13, pp. 917-930, 2006.
- [47] C. Tournassat, C. Lerouge, P. Blanc et al., "Cation exchanged Fe(II) and Sr compared to other divalent cations (Ca, Mg) in the bore Callovian-Oxfordian formation: Implications for porewater composition modelling," *Applied Geochemistry*, vol. 23, no. 4, pp. 641-654, 2008.
- [48] J. Hadi, C. Tournassat, and C. Lerouge, "Pitfalls in using the hexaamminecobalt method for cation exchange capacity measurements on clay minerals and clay-rocks: Redox interferences between the cationic dye and the sample," *Applied Clay Science*, vol. 119, pp. 393-400, 2016.
- [49] P. Négrel, J. Casanova, and J.-F. Aranyossy, "Strontium isotope systematics used to decipher the origin of groundwaters sampled from granitoids: The Vienne Case (France)," *Chemical Geology*, vol. 177, no. 3-4, pp. 287-308, 2001.

- [50] C. Lerouge, E. C. Gaucher, C. Tournassat et al., "Strontium distribution and origins in a natural clayey formation (Callovian-Oxfordian, Paris Basin, France): A new sequential extraction procedure," *Geochimica et Cosmochimica Acta*, vol. 74, no. 10, pp. 2926–2942, 2010.
- [51] N. Clauer, J. R. O'Neil, J. Honnorez, and M. Buatier, " $^{87}\text{Sr}/^{86}\text{Sr}$  and  $^{18}\text{O}/^{16}\text{O}$  ratios of clays from a hydrothermal area near the Galapagos rift as records of origin, crystallization temperature and fluid composition," *Marine Geology*, vol. 288, no. 1-4, pp. 32–42, 2011.
- [52] P. Négrel and E. Petelet-Giraud, "Strontium isotopes as tracers of groundwater-induced floods: The Somme case study (France)," *Journal of Hydrology*, vol. 305, no. 1-4, pp. 99–119, 2005.
- [53] P. Négrel and S. Roy, "Chemistry of rainwater in the Massif Central (France): A strontium isotope and major element study," *Applied Geochemistry*, vol. 13, no. 8, pp. 941–952, 1998.
- [54] P. Négrel and H. Pauwels, "Interaction between different groundwaters in Brittany catchments (France): Characterizing multiple sources through strontium- and sulphur isotope tracing," *Water, Air, & Soil Pollution*, vol. 151, no. 1-4, pp. 261–285, 2004.
- [55] F. Akagawa, H. Yoshida, S. Yogo, and K. Yamamoto, "Redox front formation in fractured crystalline rock: An analogue of matrix diffusion in an oxidizing front along water-conducting fractures," *Geochemistry: Exploration, Environment, Analysis*, vol. 6, no. 1, pp. 49–56, 2006.
- [56] H. Yoshida, K. Yamamoto, S. Yogo, and Y. Murakami, "An analogue of matrix diffusion enhanced by biogenic redox reaction in fractured sedimentary rock," *Journal of Geochemical Exploration*, vol. 90, no. 1-2, pp. 134–142, 2006.
- [57] J. C. Robinet, P. Sardini, M. Siitari-Kauppi, D. Prêt, and B. Yven, "Upscaling the porosity of the Callovo-Oxfordian mudstone from the pore scale to the formation scale; insights from the 3H-PMMA autoradiography technique and SEM BSE imaging," *Sedimentary Geology*, vol. 321, pp. 1–10, 2015.
- [58] M. E. Houben, G. Desbois, and J. L. Urai, "Pore morphology and distribution in the Shaly facies of Opalinus Clay (Mont Terri, Switzerland): Insights from representative 2D BIB-SEM investigations on mm to nm scale," *Applied Clay Science*, vol. 71, pp. 82–97, 2013.
- [59] A. G. Corkum and C. D. Martin, "The mechanical behaviour of weak mudstone (Opalinus Clay) at low stresses," *International Journal of Rock Mechanics and Mining Sciences*, vol. 44, no. 2, pp. 196–209, 2007.
- [60] M. A. Czerewko, S. A. Cross, P. G. Dumelow, and A. Saadvandi, "Assessment of pyritic Lower Lias mudrocks for earthworks," *Proceedings of the Institution of Civil Engineers: Geotechnical Engineering*, vol. 164, no. 2, pp. 59–77, 2011.
- [61] N. Hartog, J. Griffioen, and C. H. Van der Weijden, "Distribution and reactivity of  $\text{O}_2$ -reducing components in sediments from a layered aquifer," *Environmental Science & Technology*, vol. 36, no. 11, pp. 2338–2344, 2002.
- [62] G. Sposito, *The Surface Chemistry of Soils*, Oxford University Press, New York, NY, USA, 1984.
- [63] C. Tournassat, A. Vinsot, E. C. Gaucher, and S. Altmann, "chemical conditions in clay-rocks," in *Natural and Engineered Clay Barriers*, S. C. I. Tournassat, I. C. Bourg, and F. Bergaya, Eds., Developments in Clay science, 2015.
- [64] E. C. Gaucher, C. Tournassat, F. J. Pearson et al., "A robust model for pore-water chemistry of clayrock," *Geochimica et Cosmochimica Acta*, vol. 73, no. 21, pp. 6470–6487, 2009.
- [65] P. Wersin, M. Mazurek, U. K. Mäder et al., "Constraining pore-water chemistry in a 250 m thick argillaceous rock sequence," *Chemical Geology*, vol. 434, pp. 43–61, 2016.
- [66] C. Lerouge, M. Blessing, C. Flehoc et al., "Dissolved  $\text{CO}_2$  and Alkane Gas in Clay Formations," *Procedia Earth and Planetary Science*, vol. 13, pp. 88–91, 2015.



# Hindawi

Submit your manuscripts at  
<https://www.hindawi.com>

